

High-order finite-difference entropy stable schemes for two-fluid relativistic plasma flow equations

Deepak Bhoriya[†], Harish Kumar[†], and Praveen Chandrashekar[‡]

[†]Department of Mathematics, Indian Institute of Technology Delhi, New Delhi, India

[‡]Centre for Applicable Mathematics, Tata Institute of Fundamental Research,
Bangalore, India

Contents

1	Introduction	2
2	Two-fluid relativistic plasma flow equations	3
3	Analysis of continuous problem	5
4	Semi-discrete entropy stable schemes	8
4.1	Entropy stable numerical schemes for the fluid equations	8
4.1.1	High-order entropy conservative schemes for fluid equations	9
4.1.2	High-order entropy stable schemes for fluid equations	12
4.2	Discretization of Maxwell's equations	13
5	Fully discrete scheme	13
5.1	Explicit schemes	14
5.2	ARK-IMEX schemes	14
5.2.1	Second order time discretization.	15
5.2.2	Third and fourth-order time discretization.	15
6	Numerical results	15
6.1	One-dimensional test cases	16
6.1.1	Accuracy test	16
6.1.2	Relativistic Brio–Wu test problem with finite plasma skin depth	17
6.1.3	Self-similar current sheet with finite resistivity	21
6.2	Two-dimensional test cases	22
6.2.1	Relativistic Orzag-Tang test case	22
6.2.2	Relativistic two-fluid blast problem	22
6.2.3	Relativistic two-fluid GEM challenge problem	25
7	Conclusion	30
A	Barth scaling of right eigenvectors	36
A.1	Right eigenvectors	36
A.2	Barth scaling and entropy scaled right eigenvectors	37

Abstract

In this article, we propose high-order finite-difference entropy stable schemes for the two-fluid relativistic plasma flow equations. This is achieved by exploiting the structure of the equations, which consists of three independent flux components. The first two components describe the ion and electron flows, which are modeled using the relativistic hydrodynamics equation. The third component is Maxwell's equations, which are linear systems. The coupling of the ion and electron flows, and electromagnetic fields is via source terms only. Furthermore, we also show that the source terms do not affect the entropy evolution. To design semi-discrete entropy stable schemes, we extend the RHD entropy stable schemes in [1] to three dimensions. This is then coupled with entropy stable discretization of the Maxwell's equations. Finally, we use SSP-RK schemes to discretize in time. We also propose ARK-IMEX schemes to treat the stiff source terms; the resulting nonlinear set of algebraic equations is local (at each discretization point). These equations are solved using the Newton's Method, which results in an efficient method. The proposed schemes are then tested using various test problems to demonstrate their stability, accuracy and efficiency.

Keywords: Finite-difference entropy stable schemes, two-fluid relativistic plasma flows, balance laws, IMEX-schemes

1 Introduction

Relativistic plasma flows play a central role in astrophysics. In these flows, fluids moving with the speed comparable to the speed of light interact with electric and magnetic fields. Some examples are pulsar winds, gamma-ray bursts, relativistic jets from active galactic nuclei, and quasars [2], [3], [4], [5]. To model relativistic plasma flows, often, equations of relativistic Magneto-hydrodynamics (RMHD) are used [6], [7], [8], [9], [10], [11]. However, RMHD has limitations when modeling several astrophysical systems, like pulsar, gamma-ray burst, etc., see [12] for a detailed discussion. Following the development of non-relativistic two-fluid plasma flow equations [13], [14], [15], [16], [17], [18], [19], several authors have considered an analogous relativistic two-fluid plasma flow equations [20], [21], [22], [23], [24].

Two-fluid relativistic plasma flow equations describe each fluid (ion and electron) in plasma using the equations of special relativistic hydrodynamics (RHD). The fluid components are coupled via electromagnetic quantities using Lorentz force terms. Finally, the electric and magnetic fields are evolved using Maxwell's equations, where current and charges are described using fluid variables. The resulting set of PDEs is a Hyperbolic system of Balance laws with nonlinear flux and stiff source. Due to nonlinearity in the flux, the solutions will exhibit discontinuities [25]. Hence, we need to consider the weak solutions, which can be characterized using the Rankine-Hugoniot condition across the discontinuities. As the weak solutions are non-unique, entropy inequality is imposed to avoid nonphysical solutions. More recently, even the entropy solutions for the systems have been shown to be non-unique [26], still, entropy stability is one of the few nonlinear stability estimates for the solutions, and hence it is desirable to have a numerical scheme which replicates this stability at the discrete level.

As the flux and source terms are nonlinear, in general, it is not possible to find an analytical solution for the two-fluid relativistic plasma flow equations. Hence, the development of stable, efficient and accurate numerical methods is highly desirable. However, in addition to the well-known difficulties in designing stable numerical schemes for hyperbolic balance laws [27], [25], there are several additional challenges in designing such a scheme for two-fluid relativistic plasma flow equations. First, we need to compute the primitive variables from the conservative variables as the analytical expressions are not available. Second, we must satisfy additional constraints for the magnetic and electric fields. Third, we have nonlinear stiff source terms, and a suitable time implicit treatment of such source is highly desirable. Furthermore, as discussed above, it is also desirable to have entropy stability of the scheme.

Given these difficulties, there are few numerical methods for the two-fluid relativistic plasma flow model. In [28], authors have simulated the relativistic magnetic reconnection problem by assuming the symmetric motions of the fluid species, which was further improved in [20] to include the independent motion of the two-fluid species under a guide field. In [22], authors used one-dimensional two-fluid

relativistic plasma flow system to investigate the importance of the electric-field-dominated regime in the dynamics of a strongly magnetized plasma by simulating a standing shock front. In [23], authors presented a third-order accurate explicit multidimensional numerical scheme for special relativistic two-fluid plasma flow equations. Here, the authors used the method of generalized Lagrange multiplier to keep the divergence error small. Divergence-free and constraint preserving multidimensional scheme has been designed in [12, 29].

In this article, we propose arbitrarily high-order finite-difference entropy stable schemes for the relativistic two-fluid plasma flow model. High order finite-difference entropy stable schemes for general hyperbolic systems were first proposed in [30, 31]. Recently, several authors have developed entropy stable finite-difference scheme for non-relativistic fluids and plasma flows [15], [32], [33], [34]. For the relativistic fluids, Duan *et.al* [35], Biswas [36], and Bhoriya *et.al* [1] have proposed entropy stable schemes.

We proceed as follows.

- We first present the entropy framework for the two-fluid relativistic plasma flow equations. We also prove that the source terms do not affect entropy evolution.
- To design entropy stable scheme, we exploit the structure of the flux. Similar to the case of [15], the flux consists of three independent blocks. For the fluid parts, we extend the entropy conservative schemes of [1] to include a three-dimensional velocity field for each fluid component. This is then coupled with a Rusanov's solver based on higher-order Maxwell's discretization. The resultant scheme is then shown to be entropy conservative.
- To make the scheme entropy stable, following [30], [15], [1], we design high-order diffusion operator, for each component. As the source does not affect entropy evolution, the semi-discrete scheme is then shown to be entropy stable.
- As the source terms are stiff, in addition to the explicit Runge-Kutta method, we also propose IMEX schemes for the model, where flux contributions are treated explicitly, and the source is treated implicitly. The resulting set of nonlinear algebraic equations is local in each cell and are solved using Newton's method for nonlinear systems.

The rest of the article is organized as follows. In Section (2), we describe the two-fluid relativistic plasma flow equations. In Section (3), we discuss hyperbolicity and the entropy framework for the model. In Section (4), we propose semi-discrete entropy stable numerical schemes for the model. This includes the derivation of the fluid entropy conservative numerical flux and the construction of the high-order entropy diffusion operators. We also describe the discretization of the Maxwell's equations. In Section (5), we present the fully discrete scheme using time explicit and IMEX schemes. In Section (6), we provide detailed numerical tests in one and two dimensions.

2 Two-fluid relativistic plasma flow equations

The two-fluid relativistic plasma flows consists of electrons and ions, whose flows are governed by the equations of special relativistic flows. The macroscopic variables for the fluids parts are density, fluid velocity and pressure, denoted by ρ_α , \mathbf{u}_α , and p_α , respectively with $\alpha \in \{i, e\}$. Here, the subscripts $\{i, e\}$ denote the variables corresponding to the ion and electron species. These are coupled to Maxwell's

equations via source terms. The complete system is given as follows:

$$\frac{\partial(\rho_i \Gamma_i)}{\partial t} + \nabla \cdot (\rho_i \Gamma_i \mathbf{u}_i) = 0, \quad (1a)$$

$$\frac{\partial(\rho_i h_i \Gamma_i^2 \mathbf{u}_i)}{\partial t} + \nabla \cdot (\rho_i h_i \Gamma_i^2 \mathbf{u}_i \mathbf{u}_i^\top + p_i \mathbf{I}) = r_i \Gamma_i \rho_i (\mathbf{E} + \mathbf{u}_i \times \mathbf{B}), \quad (1b)$$

$$\frac{\partial(\mathcal{E}_i)}{\partial t} + \nabla \cdot ((\mathcal{E}_i + p_i) \mathbf{u}_i) = r_i \Gamma_i \rho_i (\mathbf{u}_i \cdot \mathbf{E}), \quad (1c)$$

$$\frac{\partial(\rho_e \Gamma_e)}{\partial t} + \nabla \cdot (\rho_e \Gamma_e \mathbf{u}_e) = 0, \quad (1d)$$

$$\frac{\partial(\rho_e h_e \Gamma_e^2 \mathbf{u}_e)}{\partial t} + \nabla \cdot (\rho_e h_e \Gamma_e^2 \mathbf{u}_e \mathbf{u}_e^\top + p_e \mathbf{I}) = r_e \Gamma_e \rho_e (\mathbf{E} + \mathbf{u}_e \times \mathbf{B}), \quad (1e)$$

$$\frac{\partial(\mathcal{E}_e)}{\partial t} + \nabla \cdot ((\mathcal{E}_e + p_e) \mathbf{u}_e) = r_e \Gamma_e \rho_e (\mathbf{u}_e \cdot \mathbf{E}), \quad (1f)$$

$$\frac{\partial \mathbf{B}}{\partial t} + \nabla \times \mathbf{E} = 0, \quad (1g)$$

$$\frac{\partial \mathbf{E}}{\partial t} - \nabla \times \mathbf{B} = -\mathbf{j}, \quad (1h)$$

$$\nabla \cdot \mathbf{E} = \rho_c, \quad (1i)$$

$$\nabla \cdot \mathbf{B} = 0, \quad (1j)$$

where, $\mathcal{E}_\alpha = \rho_\alpha h_\alpha \Gamma_\alpha^2 - p_\alpha$ are the energy densities, h_α are the specific enthalpy, Γ_α are the Lorentz factors, given by $\Gamma_\alpha = \frac{1}{\sqrt{1 - \mathbf{u}_\alpha^2}}$, $\mathbf{B} = (B_x, B_y, B_z)$ is the magnetic field vector, and $\mathbf{E} = (E_x, E_y, E_z)$ is the electric field vector. We have assumed the speed of light to be unity. We use notations, q_α for the particle charge and m_α for the particle mass, while the charge to mass ratios is denoted by $r_\alpha = \frac{q_\alpha}{m_\alpha}$, $\alpha \in \{i, e\}$. The total charge density ρ_c and the current density vector $\mathbf{j} = (j_x, j_y, j_z)$ are given by

$$\rho_c = r_i \rho_i \Gamma_i + r_e \rho_e \Gamma_e, \quad \mathbf{j} = r_i \rho_i \Gamma_i \mathbf{u}_i + r_e \rho_e \Gamma_e \mathbf{u}_e.$$

The above system of equations is closed using the equation of state, $h_\alpha = h_\alpha(p_\alpha, \rho_\alpha)$, where we use the ideal equation of state for h_α , which is given by

$$h_\alpha = 1 + \frac{\gamma_\alpha}{\gamma_\alpha - 1} \frac{p_\alpha}{\rho_\alpha},$$

where, $\gamma_\alpha = c_{p_\alpha}/c_{v_\alpha}$ is the ratio of specific heats. Accordingly, the polytropic index n_α , and the sound speed $c_\alpha = c_{s_\alpha}$ can be written as

$$n_\alpha = k_\alpha - 1 \quad \text{and} \quad c_\alpha^2 = \frac{k_\alpha p_\alpha}{n_\alpha \rho_\alpha h_\alpha},$$

68 where $k_\alpha = \frac{\gamma_\alpha}{\gamma_\alpha - 1}$ are constants.

69 Equations (1a) and (1d) are mass conservation laws for ion and electrons. Similarly, Equations (1b)
70 and (1e) represent momentum balance, where source terms are due to Lorentz force acting on the fluid
71 due to the electromagnetic variables. The energy conservation equations for ion and electron fluids
72 are (1c) and (1f), respectively. Here, source terms are kinetic energy contributions due to electric and
73 magnetic fields. Equations (1g)-(1j) are Maxwell's equations, describing the constraint evolution of the
74 electric and magnetic fields.

75 Usually, to deal with the constraints (1i) and (1j) in plasma flow models [15], a hyperbolic form
76 of Maxwell's equations [37] is considered. However, we did not observe any difference in the numerical
77 results if we consider the Hyperbolic formulation of the equations. Furthermore, more suitable methods
78 are presented in [12, 29]. Hence, we have ignored these constraint equations.

3 Analysis of continuous problem

Let us introduce the notations, $D_\alpha = \Gamma_\alpha \rho_\alpha$ and $\mathbf{M}_\alpha = (M_{x_\alpha}, M_{y_\alpha}, M_{z_\alpha}) = \rho_\alpha h_\alpha \Gamma_\alpha^2 \mathbf{u}_\alpha$ for $\alpha \in \{i, e\}$. The vector of conservative variables \mathbf{U} can be written as,

$$\mathbf{U} = (\mathbf{U}_i^\top, \mathbf{U}_e^\top, \mathbf{U}_m^\top)^\top,$$

where $\mathbf{U}_i = (D_i, \mathbf{M}_i, \mathcal{E}_i)^\top$ are ion fluid variables, $\mathbf{U}_e = (D_e, \mathbf{M}_e, \mathcal{E}_e)^\top$ are electron fluid variables, and $\mathbf{U}_m = (\mathbf{B}, \mathbf{E})^\top$ are Maxwell's variables. In two dimensions, let us also denote x - and y -directional fluxes as \mathbf{f}^x and \mathbf{f}^y , respectively. From (1), expressions for the fluxes can be written as,

$$\mathbf{f}^x = \begin{pmatrix} \mathbf{f}_i^x(\mathbf{U}_i) \\ \mathbf{f}_e^x(\mathbf{U}_e) \\ \mathbf{f}_m^x(\mathbf{U}_m) \end{pmatrix}, \quad \text{and} \quad \mathbf{f}^y = \begin{pmatrix} \mathbf{f}_i^y(\mathbf{U}_i) \\ \mathbf{f}_e^y(\mathbf{U}_e) \\ \mathbf{f}_m^y(\mathbf{U}_m) \end{pmatrix},$$

where

$$\mathbf{f}_\alpha^x = \begin{pmatrix} D_\alpha u_{x_\alpha} \\ M_{x_\alpha} u_{x_\alpha} + p_\alpha \\ M_{y_\alpha} u_{x_\alpha} \\ M_{z_\alpha} u_{x_\alpha} \\ M_{x_\alpha} \end{pmatrix}, \quad \text{and} \quad \mathbf{f}_\alpha^y = \begin{pmatrix} D_\alpha u_{y_\alpha} \\ M_{x_\alpha} u_{y_\alpha} \\ M_{y_\alpha} u_{y_\alpha} + p_\alpha \\ M_{z_\alpha} u_{y_\alpha} \\ M_{y_\alpha} \end{pmatrix}, \quad (2)$$

for the flow parts and

$$\mathbf{f}_m^x = \begin{pmatrix} 0 \\ -E_z \\ E_y \\ 0 \\ B_z \\ -B_y \end{pmatrix}, \quad \text{and} \quad \mathbf{f}_m^y = \begin{pmatrix} E_z \\ 0 \\ -E_x \\ -B_z \\ 0 \\ B_x \end{pmatrix}, \quad (3)$$

for the Maxwell's part. We note that the flux for the whole system contains three independent parts, two fluid parts modeled using the equations of special relativistic flows, and the third part is linear Maxwell's flux. These three parts are coupled via source terms, which are given as,

$$\mathbf{s} = \begin{pmatrix} \mathbf{s}_i(\mathbf{U}_i, \mathbf{U}_m) \\ \mathbf{s}_e(\mathbf{U}_e, \mathbf{U}_m) \\ \mathbf{s}_m(\mathbf{U}_i, \mathbf{U}_e) \end{pmatrix},$$

where,

$$\mathbf{s}_\alpha = \begin{pmatrix} 0 \\ r_\alpha D_\alpha (E_x + u_{y_\alpha} B_z - u_{z_\alpha} B_y) \\ r_\alpha D_\alpha (E_y + u_{z_\alpha} B_x - u_{x_\alpha} B_z) \\ r_\alpha D_\alpha (E_z + u_{x_\alpha} B_y - u_{y_\alpha} B_x) \\ r_\alpha D_\alpha (u_{x_\alpha} E_x + u_{y_\alpha} E_y + u_{z_\alpha} E_z) \end{pmatrix}, \quad \text{and} \quad \mathbf{s}_m = \begin{pmatrix} 0 \\ 0 \\ 0 \\ -j_x \\ -j_y \\ -j_z \end{pmatrix},$$

for $\alpha \in \{i, e\}$. Using the above notations, the system (1), for the two-dimensional case can be written in the conservation form as follows:

$$\frac{\partial \mathbf{U}}{\partial t} + \frac{\partial \mathbf{f}^x}{\partial x} + \frac{\partial \mathbf{f}^y}{\partial y} = \mathbf{s}. \quad (4)$$

Let us also introduce the vector of primitive variables $\mathbf{W} = (\mathbf{W}_i^\top, \mathbf{W}_e^\top, \mathbf{W}_m^\top)^\top$, where $\mathbf{W}_\alpha = (\rho_\alpha, \mathbf{u}_\alpha, p_\alpha)^\top$ and $\mathbf{W}_m = (\mathbf{B}, \mathbf{E})^\top$. We follow the procedure given in [1, 38] to extract the primitive variables from the conservative variables. We define the set of admissible solution space

$$\Omega = \{\mathbf{U} \in \mathbb{R}^{16} : \rho_i > 0, \rho_e > 0, p_i > 0, p_e > 0, |\mathbf{u}_i| < 1, |\mathbf{u}_e| < 1\}.$$

The eigenvalues of the system in x -direction are,

$$\Lambda^x = \left\{ \frac{(1 - c_i^2)u_{x_i} - (c_i/\Gamma_i)\sqrt{Q_i^x}}{1 - c_i^2|\mathbf{u}_i|^2}, u_{x_i}, u_{x_i}, u_{x_i}, \frac{(1 - c_i^2)u_{x_i} + (c_i/\Gamma_i)\sqrt{Q_i^x}}{1 - c_i^2|\mathbf{u}_i|^2}, \right. \\ \left. \frac{(1 - c_e^2)u_{x_e} - (c_e/\Gamma_e)\sqrt{Q_e^x}}{1 - c_e^2|\mathbf{u}_e|^2}, u_{x_e}, u_{x_e}, u_{x_e}, \frac{(1 - c_e^2)u_{x_e} + (c_e/\Gamma_e)\sqrt{Q_e^x}}{1 - c_e^2|\mathbf{u}_e|^2}, \right. \\ \left. -1, -1, 0, 0, 1, 1 \right\},$$

80 where, $Q_\alpha^x = 1 - u_{x_\alpha}^2 - c_\alpha^2(u_{y_\alpha}^2 + u_{z_\alpha}^2)$, $\alpha \in \{i, e\}$. For $\mathbf{U} \in \Omega$ and $\gamma_\alpha \in (1, 2]$ we have $c_\alpha < 1$ which
 81 implies that $Q_\alpha^x > 0$, hence all the eigenvalues are real. The complete set of right eigenvectors for the
 82 Jacobian matrix $\frac{\partial \mathbf{f}^x}{\partial \mathbf{U}}$ is given in Appendix (A.1). The Appendix also contains the eigenvalues and right
 83 eigenvectors for the jacobian matrix $\frac{\partial \mathbf{f}^y}{\partial \mathbf{U}}$. Consequently, we can state the following Lemma.

84 **Lemma 3.1.** *The system (4) is hyperbolic for the states $\mathbf{U} \in \Omega$, with real eigenvalues and a complete*
 85 *set of eigenvectors.*

We now introduce entropy functions for the two-fluid relativistic plasma flow equations. The entropy functions \mathcal{U}_α and associated entropy fluxes \mathcal{F}_α^d for the fluid part of the system (4) are given by,

$$\mathcal{U}_\alpha = -\frac{\rho_\alpha \Gamma_\alpha s_\alpha}{\gamma_\alpha - 1} \quad \text{and} \quad \mathcal{F}_\alpha^d = -\frac{\rho_\alpha \Gamma_\alpha s_\alpha u_{d_\alpha}}{\gamma_\alpha - 1}, \quad \alpha \in \{i, e\}, \quad d = x, y.$$

Here, $s_\alpha = \ln(p_\alpha \rho_\alpha^{-\gamma_\alpha})$. The pair $(\mathcal{U}_\alpha, \mathcal{F}_\alpha^d)$ is called an *entropy-entropy flux pair*. For simplicity, we only consider the one-dimensional case, i.e.,

$$\frac{\partial \mathbf{U}}{\partial t} + \frac{\partial \mathbf{f}^x}{\partial x} = \mathbf{s}. \quad (5)$$

86 The extension of entropy framework to higher dimensions is straightforward. We will now prove the
 87 following result:

Proposition 3.1. *The smooth solutions of (5) satisfy the entropy equality,*

$$\partial_t s_\alpha + u_{x_\alpha} \partial_x s_\alpha = 0, \quad \alpha \in \{i, e\}.$$

As a consequence, every smooth function $H(s_\alpha)$ of s_α satisfies

$$\partial_t(\rho_\alpha \Gamma_\alpha H(s_\alpha)) + \partial_x(\rho_\alpha \Gamma_\alpha u_{x_\alpha} H(s_\alpha)) = 0. \quad (6)$$

In particular, we have the following entropy equality for the smooth solutions,

$$\partial_t \mathcal{U}_\alpha + \partial_x \mathcal{F}_\alpha^x = 0. \quad (7)$$

88 We will give the proof of Proposition (3.1) in two steps. Firstly, we will prove two lemmas, and
 89 then we give the proof of proposition using these two lemmas. The proof is similar to those in [1] for
 90 relativistic hydrodynamics except for the additional source terms and three-dimensional velocity field.

Lemma 3.2. *The smooth solutions of the system (5) satisfies the following identity*

$$\frac{1}{\Gamma_\alpha^2} \partial_t p_\alpha = \partial_t p_\alpha + u_{x_\alpha} \partial_x p_\alpha + \left(\frac{\rho_\alpha h_\alpha}{\Gamma_\alpha} \right) (\partial_t \Gamma_\alpha + \partial_x (\Gamma_\alpha u_{x_\alpha})) - \rho_\alpha h_\alpha \partial_x u_{x_\alpha} - \mathbf{u}_\alpha \cdot (\mathbf{s}_{\mathbf{M}_\alpha} - \mathbf{u}_\alpha \mathbf{s}_{\mathcal{E}_\alpha}), \quad (8)$$

where

$$\mathbf{s}_{\mathbf{M}_\alpha} = r_\alpha \Gamma_\alpha \rho_\alpha (\mathbf{E} + \mathbf{u}_\alpha \times \mathbf{B}), \quad \mathbf{s}_{\mathcal{E}_\alpha} = r_\alpha \Gamma_\alpha \rho_\alpha (\mathbf{u}_\alpha \cdot \mathbf{E}).$$

91 are the source terms in the momentum and energy equations.

Proof. Let \mathbf{U} be the smooth solution of the system (5). Then we can write,

$$\partial_t(\rho_\alpha \Gamma_\alpha) + \partial_x(\rho_\alpha \Gamma_\alpha u_{x_\alpha}) = 0, \quad (9)$$

$$\partial_t(\rho_\alpha h_\alpha \Gamma_\alpha^2 u_{x_\alpha}) + \partial_x(\rho_\alpha h_\alpha \Gamma_\alpha^2 u_{x_\alpha}^2) + \partial_x p_\alpha = \mathbf{s}_{M_{x_\alpha}}, \quad (10)$$

$$\partial_t(\rho_\alpha h_\alpha \Gamma_\alpha^2 u_{y_\alpha}) + \partial_x(\rho_\alpha h_\alpha \Gamma_\alpha^2 u_{x_\alpha} u_{y_\alpha}) = \mathbf{s}_{M_{y_\alpha}}, \quad (11)$$

$$\partial_t(\rho_\alpha h_\alpha \Gamma_\alpha^2 u_{z_\alpha}) + \partial_x(\rho_\alpha h_\alpha \Gamma_\alpha^2 u_{x_\alpha} u_{z_\alpha}) = \mathbf{s}_{M_{z_\alpha}}, \quad (12)$$

$$\partial_t(\rho_\alpha h_\alpha \Gamma_\alpha^2) - \partial_t(p_\alpha) + \partial_x(\rho_\alpha h_\alpha \Gamma_\alpha^2 u_{x_\alpha}) = \mathbf{s}_{\mathcal{E}_\alpha}, \quad (13)$$

where, we have used $\mathbf{s}_{M_\alpha} = (\mathbf{s}_{M_{x_\alpha}}, \mathbf{s}_{M_{y_\alpha}}, \mathbf{s}_{M_{z_\alpha}})$, as the momentum source vector, i.e., source terms of the Eqns. (1b) and (1e). Also, $\mathbf{s}_{\mathcal{E}_\alpha}$ is the source term of the energy equations (1c), and (1f). We apply the product rule on Equations (10)-(12) and substitute the value of $\partial_x(\rho_\alpha h_\alpha \Gamma_\alpha^2 u_{x_\alpha})$ from Eqn. (13) in each of the three equations to obtain the following set of three identities:

$$(\rho_\alpha h_\alpha \Gamma_\alpha^2 u_{x_\alpha})(\partial_t u_{x_\alpha} + u_{x_\alpha} \partial_x u_{x_\alpha}) + u_{x_\alpha}^2 \partial_t p_\alpha + u_{x_\alpha} \partial_x p_\alpha = u_{x_\alpha} (\mathbf{s}_{M_{x_\alpha}} - u_{x_\alpha} \mathbf{s}_{\mathcal{E}_\alpha}) \quad (14a)$$

$$(\rho_\alpha h_\alpha \Gamma_\alpha^2 u_{y_\alpha})(\partial_t u_{y_\alpha} + u_{y_\alpha} \partial_x u_{y_\alpha}) + u_{y_\alpha}^2 \partial_t p_\alpha = u_{y_\alpha} (\mathbf{s}_{M_{y_\alpha}} - u_{y_\alpha} \mathbf{s}_{\mathcal{E}_\alpha}) \quad (14b)$$

$$(\rho_\alpha h_\alpha \Gamma_\alpha^2 u_{z_\alpha})(\partial_t u_{z_\alpha} + u_{z_\alpha} \partial_x u_{z_\alpha}) + u_{z_\alpha}^2 \partial_t p_\alpha = u_{z_\alpha} (\mathbf{s}_{M_{z_\alpha}} - u_{z_\alpha} \mathbf{s}_{\mathcal{E}_\alpha}) \quad (14c)$$

We observe that $\partial_t \Gamma_\alpha = \Gamma_\alpha^3 \mathbf{u}_\alpha \cdot \partial_t \mathbf{u}_\alpha$, and $\partial_x \Gamma_\alpha = \Gamma_\alpha^3 \mathbf{u}_\alpha \cdot \partial_x \mathbf{u}_\alpha$. Consequently, Eqn. (14a) simplifies to

$$\begin{aligned} \left(\frac{\rho_\alpha h_\alpha}{\Gamma_\alpha} \right) (\partial_t \Gamma_\alpha + u_{x_\alpha} \partial_x \Gamma_\alpha) - \rho_\alpha h_\alpha \Gamma_\alpha^2 u_{y_\alpha} (\partial_t u_{y_\alpha} + u_{x_\alpha} \partial_x u_{y_\alpha}) - \rho_\alpha h_\alpha \Gamma_\alpha^2 u_{z_\alpha} (\partial_t u_{z_\alpha} + u_{x_\alpha} \partial_x u_{z_\alpha}) \\ + u_{x_\alpha}^2 \partial_t p_\alpha + u_{x_\alpha} \partial_x p_\alpha = u_{x_\alpha} (\mathbf{s}_{M_{x_\alpha}} - u_{x_\alpha} \mathbf{s}_{\mathcal{E}_\alpha}), \end{aligned} \quad (15)$$

92 From the definition of Lorentz factor Γ_α , we have $u_{x_\alpha}^2 = 1 - \frac{1}{\Gamma_\alpha^2} - u_{y_\alpha}^2 - u_{z_\alpha}^2$. We substitute this value of
93 $u_{x_\alpha}^2$ in Eqn. (15), followed by the substitution of value of $u_{y_\alpha}^2 \partial_t p_\alpha$ and $u_{z_\alpha}^2 \partial_t p_\alpha$ from the Eqn. (14b)-(14c),
94 to obtain the required identity (8). \square

Lemma 3.3. *For smooth solutions of the system (5), we have the following identity*

$$(\partial_t p_\alpha + u_{x_\alpha} \partial_x p_\alpha) + \frac{p_\alpha \gamma_\alpha}{\Gamma_\alpha} (\partial_t \Gamma_\alpha + \partial_x (\Gamma_\alpha u_{x_\alpha})) = 0. \quad (16)$$

Proof. We expand Eqn. (13) using the product rule and simplify further using the substitution of variables from Eqn. (9) to obtain,

$$\begin{aligned} \partial_t p_\alpha + u_{x_\alpha} \partial_x p_\alpha = \left(\frac{\gamma_\alpha - 1}{\Gamma_\alpha^2 \gamma_\alpha} \right) \mathbf{s}_{\mathcal{E}_\alpha} + \left(\frac{\gamma_\alpha - 1}{\Gamma_\alpha^2 \gamma_\alpha} \right) \partial_t p_\alpha - \left(\frac{\rho_\alpha \gamma_\alpha - 1}{\Gamma_\alpha \gamma_\alpha} \right) (\partial_t \Gamma_\alpha + \partial_x (\Gamma_\alpha u_{x_\alpha})) \\ - 2(\partial_t \Gamma_\alpha + \partial_x (\Gamma_\alpha u_{x_\alpha})) \frac{p_\alpha}{\Gamma_\alpha} + \rho_\alpha \left(\frac{\gamma_\alpha - 1}{\gamma_\alpha} \right) \partial_x u_{x_\alpha} + p_\alpha \partial_x u_{x_\alpha}. \end{aligned} \quad (17)$$

Substituting the value of $\frac{1}{\Gamma_\alpha^2} \partial_t p_\alpha$ from the identity of Lemma (3.2), and simplifying further we get

$$\begin{aligned} \partial_t p_\alpha + u_{x_\alpha} \partial_x p_\alpha = \left(\frac{\gamma_\alpha - 1}{\gamma_\alpha} \right) \left(-\mathbf{u}_\alpha \cdot \mathbf{s}_{M_\alpha} + \left(\frac{1 + \mathbf{u}_\alpha^2}{\Gamma_\alpha^2} \right) \mathbf{s}_{\mathcal{E}_\alpha} \right) \\ + \left(\frac{\gamma_\alpha - 1}{\gamma_\alpha} \right) (\partial_t p_\alpha + u_{x_\alpha} \partial_x p_\alpha) \\ + \left(\frac{\gamma_\alpha - 1}{\gamma_\alpha} \right) \left[\left(\frac{\rho_\alpha h_\alpha}{\Gamma_\alpha} \right) (\partial_t \Gamma_\alpha + \partial_x (\Gamma_\alpha u_{x_\alpha})) - \rho_\alpha h_\alpha \partial_x u_{x_\alpha} \right] \\ - \left(\frac{\rho_\alpha \gamma_\alpha - 1}{\Gamma_\alpha \gamma_\alpha} \right) (\partial_t \Gamma_\alpha + \partial_x (\Gamma_\alpha u_{x_\alpha})) - \frac{2p_\alpha}{\Gamma_\alpha} (\partial_t \Gamma_\alpha + \partial_x (\Gamma_\alpha u_{x_\alpha})) \\ + \left(\frac{\gamma_\alpha - 1}{\gamma_\alpha} \right) \rho_\alpha \partial_x u_{x_\alpha} + p_\alpha \partial_x u_{x_\alpha}, \end{aligned}$$

95 We observe that $\mathbf{u}_\alpha \cdot \mathbf{s}_{M_\alpha} - \mathbf{s}_{\mathcal{E}_\alpha} = 0$, thus, after further simplifications and cancellations [1], we obtain (16).
96 \square

Proof of Proposition (3.1). We find the partial derivatives of $s_\alpha = \ln(p_\alpha \rho_\alpha^{-\gamma_\alpha})$ with respect to t and x , to obtain

$$\partial_t s_\alpha = \frac{1}{p_\alpha} \partial_t p_\alpha - \frac{\gamma_\alpha}{\rho_\alpha} \partial_t \rho_\alpha \quad \text{and} \quad \partial_x s_\alpha = \frac{1}{p_\alpha} \partial_x p_\alpha - \frac{\gamma_\alpha}{\rho_\alpha} \partial_x \rho_\alpha. \quad (18)$$

Once we have the partial derivatives, we apply the product rule on the mass density Eqn. (9) to obtain an identity in terms of the partial derivatives of ρ_α

$$\frac{1}{\rho_\alpha} (\partial_t \rho_\alpha + u_{x_\alpha} \partial_x \rho_\alpha) = -\frac{1}{\Gamma_\alpha} (\partial_t \Gamma_\alpha + \partial_x (\Gamma_\alpha u_{x_\alpha})). \quad (19)$$

Combining Eqn. (16) and Eqn. (19) we obtain the expression

$$\frac{1}{p_\alpha} (\partial_t p_\alpha + u_{x_\alpha} \partial_x p_\alpha) - \frac{\gamma_\alpha}{\rho_\alpha} (\partial_t \rho_\alpha + u_{x_\alpha} \partial_x \rho_\alpha) = 0,$$

which, on using Eqn. (18), is equivalent to $\partial_t s_\alpha + u_{x_\alpha} \partial_x s_\alpha = 0$. The identity (6) is a direct consequence of the product rule. To obtain the final entropy equality (7), we simplify the identity (6) by choosing particular value of $H(s_\alpha)$ as $H(s_\alpha) = \frac{-s_\alpha}{\gamma_\alpha - 1}$. \square

Remark 3.1. The entropy equality (7) in Proposition (3.1) gives rise to the entropy inequality

$$\partial_t \mathcal{U}_\alpha + \partial_x \mathcal{F}_\alpha^x \leq 0, \quad (20)$$

in the sense of distributions for non-smooth solutions.

In the above analysis, we also note that the Maxwell's flux does not affect the fluid entropies. This fact will be exploited to design semi-discrete high-order numerical schemes which will satisfy the entropy inequality (20).

4 Semi-discrete entropy stable schemes

In this section, we will design semi-discrete entropy stable numerical schemes for the two-dimensional two-fluid relativistic plasma flow Eqns. (4). The extension to three dimensions is fairly easy. Let us consider the domain $D = I_x \times I_y$, where $I_x = (x_{min}, x_{max})$ and $I_y = (y_{min}, y_{max})$. The domain D is discretized using the uniform mesh with cells of size $\Delta x \times \Delta y$. We define $x_i = x_{min} + i\Delta x$ for $0 \leq i \leq N_x$ and $y_j = y_{min} + j\Delta y$ for $0 \leq j \leq N_y$. The cell (i, j) is given by $I_{i,j} = [x_{i-1/2}, x_{i+1/2}] \times [y_{j-1/2}, y_{j+1/2}]$, where $x_{i+1/2} = \frac{x_i + x_{i+1}}{2}$ and $y_{j+1/2} = \frac{y_j + y_{j+1}}{2}$.

The semi-discrete finite difference scheme for the evolution of solution $\mathbf{U}_{i,j}$ at (x_i, y_j) of system (4) is given by,

$$\frac{d}{dt} \mathbf{U}_{i,j}(t) + \frac{1}{\Delta x} \left(\mathbf{F}_{i+\frac{1}{2},j}^x(t) - \mathbf{F}_{i-\frac{1}{2},j}^x(t) \right) + \frac{1}{\Delta y} \left(\mathbf{F}_{i,j+\frac{1}{2}}^y(t) - \mathbf{F}_{i,j-\frac{1}{2}}^y(t) \right) = \mathbf{s}(\mathbf{U}_{i,j}(t)), \quad (21)$$

where $\mathbf{F}_{i+\frac{1}{2},j}^x, \mathbf{F}_{i,j+\frac{1}{2}}^y$ are the numerical fluxes consistent with the continuous fluxes $\mathbf{f}^x, \mathbf{f}^y$, respectively.

4.1 Entropy stable numerical schemes for the fluid equations

To simplify the discussion, we will first present the discretization of the fluid part, i.e., we consider the following differential form:

$$\frac{\partial \mathbf{U}_\alpha}{\partial t} + \frac{\partial \mathbf{f}_\alpha^x}{\partial x} + \frac{\partial \mathbf{f}_\alpha^y}{\partial y} = \mathbf{s}_\alpha(\mathbf{U}_\alpha, \mathbf{U}_m), \quad (22)$$

for $\alpha \in \{i, e\}$. Let us now define:

115 **Definition 4.1.** *The numerical scheme*

$$\begin{aligned} \frac{d}{dt} \mathbf{U}_{\alpha,i,j}(t) + \frac{1}{\Delta x} \left(\mathbf{F}_{\alpha,i+\frac{1}{2},j}^x(t) - \mathbf{F}_{\alpha,i-\frac{1}{2},j}^x(t) \right) + \frac{1}{\Delta y} \left(\mathbf{F}_{\alpha,i,j+\frac{1}{2}}^y(t) - \mathbf{F}_{\alpha,i,j-\frac{1}{2}}^y(t) \right) \\ = \mathbf{s}_{\alpha}(\mathbf{U}_{\alpha,i,j}(t), \mathbf{U}_{m,i,j}(t)), \end{aligned} \quad (23)$$

is said to be entropy conservative if the following entropy equality is satisfied

$$\frac{d}{dt} \mathcal{U}_{\alpha}(\mathbf{U}_{ij}) + \frac{1}{\Delta x} \left(\hat{\mathcal{F}}_{\alpha,i+\frac{1}{2},j}^x - \hat{\mathcal{F}}_{\alpha,i-\frac{1}{2},j}^x \right) + \frac{1}{\Delta y} \left(\hat{\mathcal{F}}_{\alpha,i,j+\frac{1}{2}}^y - \hat{\mathcal{F}}_{\alpha,i,j-\frac{1}{2}}^y \right) = 0, \quad \alpha \in \{i, e\}, \quad (24)$$

116 where $\hat{\mathcal{F}}_{\alpha,i+\frac{1}{2},j}^x, \hat{\mathcal{F}}_{\alpha,i,j+\frac{1}{2}}^y$ are some numerical entropy flux functions consistent with the entropy fluxes \mathcal{F}_{α}^x ,
117 \mathcal{F}_{α}^y , respectively. Here $\mathbf{F}_{\alpha,i+\frac{1}{2},j}^x, \mathbf{F}_{\alpha,i,j+\frac{1}{2}}^y$ are the numerical fluxes consistent with $\mathbf{f}^x, \mathbf{f}^y$, respectively.

The scheme is said to be entropy stable if the following entropy inequality is satisfied:

$$\frac{d}{dt} \mathcal{U}_{\alpha}(\mathbf{U}_{\alpha,i,j}) + \frac{1}{\Delta x} \left(\hat{\mathcal{F}}_{\alpha,i+\frac{1}{2},j}^x - \hat{\mathcal{F}}_{\alpha,i-\frac{1}{2},j}^x \right) + \frac{1}{\Delta y} \left(\hat{\mathcal{F}}_{\alpha,i,j+\frac{1}{2}}^y - \hat{\mathcal{F}}_{\alpha,i,j-\frac{1}{2}}^y \right) \leq 0 \quad \alpha \in \{i, e\}, \quad (25)$$

118 To obtain the entropy stable schemes, we will first construct the entropy conservative schemes and
119 then add dissipative fluxes to obtain entropy inequality.

120 4.1.1 High-order entropy conservative schemes for fluid equations

Let us introduce *entropy variables*,

$$\mathbf{V}_{\alpha}(\mathbf{U}_{\alpha}) = \frac{\partial \mathcal{U}_{\alpha}}{\partial \mathbf{U}_{\alpha}}$$

and *entropy potentials*,

$$\psi_{\alpha}^x(\mathbf{U}_{\alpha}) = \mathbf{V}_{\alpha}^{\top}(\mathbf{U}_{\alpha}) \cdot \mathbf{f}_{\alpha}^x(\mathbf{U}_{\alpha}) - \mathcal{F}_{\alpha}^x(\mathbf{U}_{\alpha}), \quad \psi_{\alpha}^y(\mathbf{U}_{\alpha}) = \mathbf{V}_{\alpha}^{\top}(\mathbf{U}_{\alpha}) \cdot \mathbf{f}_{\alpha}^y(\mathbf{U}_{\alpha}) - \mathcal{F}_{\alpha}^y(\mathbf{U}_{\alpha})$$

for $\alpha \in \{i, e\}$. A simple calculation results in the following expressions

$$\mathbf{V}_{\alpha} = \begin{pmatrix} \frac{\gamma_{\alpha} - s_{\alpha}}{\gamma_{\alpha} - 1} + \beta_{\alpha} \\ u_{x\alpha} \Gamma_{\alpha} \beta_{\alpha} \\ u_{y\alpha} \Gamma_{\alpha} \beta_{\alpha} \\ u_{z\alpha} \Gamma_{\alpha} \beta_{\alpha} \\ -\Gamma_{\alpha} \beta_{\alpha} \end{pmatrix}, \quad \text{with} \quad \beta_{\alpha} = \frac{\rho_{\alpha}}{p_{\alpha}}, \quad (26)$$

and

$$\psi_{\alpha}^x = \rho_{\alpha} \Gamma_{\alpha} u_{x\alpha}, \quad \psi_{\alpha}^y = \rho_{\alpha} \Gamma_{\alpha} u_{y\alpha}. \quad (27)$$

We also introduce the following notations for jumps and averaging operations over the cell interfaces

$$\begin{aligned} \llbracket a \rrbracket_{i+\frac{1}{2},j} &= a_{i+1,j} - a_{i,j}, & \bar{a}_{i+\frac{1}{2},j} &= \frac{1}{2}(a_{i+1,j} + a_{i,j}), \\ \llbracket a \rrbracket_{i,j+\frac{1}{2}} &= a_{i,j+1} - a_{i,j}, & \bar{a}_{i,j+\frac{1}{2}} &= \frac{1}{2}(a_{i,j+1} + a_{i,j}). \end{aligned}$$

Let us first consider the homogeneous fluid part, i.e., we consider

$$\frac{\partial \mathbf{U}_{\alpha}}{\partial t} + \frac{\partial \mathbf{f}_{\alpha}^x}{\partial x} + \frac{\partial \mathbf{f}_{\alpha}^y}{\partial y} = 0. \quad (28)$$

121 and the corresponding semi-discrete scheme

$$\frac{d}{dt} \mathbf{U}_{\alpha,i,j}(t) + \frac{1}{\Delta x} \left(\mathbf{F}_{\alpha,i+\frac{1}{2},j}^x(t) - \mathbf{F}_{\alpha,i-\frac{1}{2},j}^x(t) \right) + \frac{1}{\Delta y} \left(\mathbf{F}_{\alpha,i,j+\frac{1}{2}}^y(t) - \mathbf{F}_{\alpha,i,j-\frac{1}{2}}^y(t) \right) = 0 \quad (29)$$

122 Then we have the following result from [39].

Theorem 4.1 (Tadmor [39]). Let $\tilde{\mathbf{F}}_\alpha^x$ and $\tilde{\mathbf{F}}_\alpha^y$ be the consistent numerical fluxes which satisfy

$$[\mathbf{V}_\alpha]_{i+\frac{1}{2},j}^\top \tilde{\mathbf{F}}_{\alpha,i+\frac{1}{2},j}^x = [\psi_\alpha^x]_{i+\frac{1}{2},j}, \quad [\mathbf{V}_\alpha]_{i,j+\frac{1}{2}}^\top \tilde{\mathbf{F}}_{\alpha,i,j+\frac{1}{2}}^y = [\psi_\alpha^y]_{i,j+\frac{1}{2}}, \quad (30)$$

then the scheme (29) with the numerical fluxes $\tilde{\mathbf{F}}_\alpha^x$ and $\tilde{\mathbf{F}}_\alpha^y$ is second order accurate and entropy conservative, i.e., the entropy equality

$$\frac{d}{dt} \mathcal{U}_\alpha(\mathbf{U}_{ij}) + \frac{1}{\Delta x} \left(\tilde{\mathcal{F}}_{\alpha,i+\frac{1}{2},j}^x - \tilde{\mathcal{F}}_{\alpha,i-\frac{1}{2},j}^x \right) + \frac{1}{\Delta y} \left(\tilde{\mathcal{F}}_{\alpha,i,j+\frac{1}{2}}^y - \tilde{\mathcal{F}}_{\alpha,i,j-\frac{1}{2}}^y \right) = 0,$$

is satisfied with the consistent entropy numerical fluxes,

$$\tilde{\mathcal{F}}_{\alpha,i+\frac{1}{2},j}^x = \bar{\mathbf{V}}_{\alpha,i+\frac{1}{2},j}^\top \tilde{\mathbf{F}}_{\alpha,i+\frac{1}{2},j}^x - \bar{\psi}_{\alpha,i+\frac{1}{2},j}^x, \quad \text{and} \quad \tilde{\mathcal{F}}_{\alpha,i,j+\frac{1}{2}}^y = \bar{\mathbf{V}}_{\alpha,i,j+\frac{1}{2}}^\top \tilde{\mathbf{F}}_{\alpha,i,j+\frac{1}{2}}^y - \bar{\psi}_{\alpha,i,j+\frac{1}{2}}^y.$$

We consider the x -directional identity of Eqn. (30) and observe that the equation (30) contains five unknowns, $\tilde{\mathbf{F}}_\alpha^x = (F_{\alpha,1}^x, F_{\alpha,2}^x, F_{\alpha,3}^x, F_{\alpha,4}^x, F_{\alpha,5}^x)^\top$. Hence, in general, we will have non-uniqueness for the solutions of this algebraic equation. Several authors [32, 40] have presented different techniques to find an affordable entropy conservative flux. We will follow the procedure of [32].

We will follow [1] to derive the following expression for the fluxes. Consider the flux at $(i + \frac{1}{2}, j)$. To simplify the notation, we suppress the cell indices i, j , and let

$$[\cdot] = (\cdot)_{i+1,j} - (\cdot)_{i,j}, \quad (\bar{\cdot}) = \frac{(\cdot)_{i,j} + (\cdot)_{i+1,j}}{2}$$

Define $a^{\text{ln}} = \frac{[a]}{[\log a]}$ as the logarithmic average for a strictly positive scalar a .

Applying the jump condition $[ab] = \bar{a}[b] + \bar{b}[a]$ on the equation $\Gamma_\alpha = \frac{1}{\sqrt{1 - \mathbf{u}_\alpha^2}}$ written as $\Gamma_\alpha^2 = 1 + m_{x_\alpha}^2 + m_{y_\alpha}^2 + m_{z_\alpha}^2$, we obtain

$$[\Gamma_\alpha] = \frac{1}{\Gamma_\alpha} (\bar{m}_{x_\alpha} [m_{x_\alpha}] + \bar{m}_{y_\alpha} [m_{y_\alpha}] + \bar{m}_{z_\alpha} [m_{z_\alpha}]),$$

where, $m_{x_\alpha} = \Gamma_\alpha u_{x_\alpha}$, $m_{y_\alpha} = \Gamma_\alpha u_{y_\alpha}$ and $m_{z_\alpha} = \Gamma_\alpha u_{z_\alpha}$. Using this, we can write the jump in \mathbf{V}_α in terms of the jump in ρ_α , β_α , m_{x_α} , m_{y_α} and m_{z_α} as follows:

$$[\mathbf{V}_\alpha] = \begin{pmatrix} \frac{[\rho_\alpha]}{\rho_\alpha^{\text{ln}}} + k_\alpha [\beta_\alpha] \\ \bar{m}_{x_\alpha} [\beta_\alpha] + \beta_\alpha [m_{x_\alpha}] \\ \bar{m}_{y_\alpha} [\beta_\alpha] + \beta_\alpha [m_{y_\alpha}] \\ \bar{m}_{z_\alpha} [\beta_\alpha] + \beta_\alpha [m_{z_\alpha}] \\ -\Gamma_\alpha [\beta_\alpha] - \frac{\bar{\beta}_\alpha \bar{m}_{x_\alpha}}{\Gamma_\alpha} [m_{x_\alpha}] - \frac{\bar{\beta}_\alpha \bar{m}_{y_\alpha}}{\Gamma_\alpha} [m_{y_\alpha}] - \frac{\bar{\beta}_\alpha \bar{m}_{z_\alpha}}{\Gamma_\alpha} [m_{z_\alpha}] \end{pmatrix},$$

where $\beta_\alpha = \frac{\rho_\alpha}{p_\alpha}$, and $k_\alpha = \left(\frac{1}{\gamma - 1} \frac{1}{\beta_\alpha^{\text{ln}}} + 1 \right)$. Furthermore, $[\psi_\alpha^x]$ can be written as

$$[\psi_\alpha^x] = \bar{\rho}_\alpha [m_{x_\alpha}] + \bar{m}_{x_\alpha} [\rho_\alpha].$$

and Eqn. (30) becomes

$$F_{\alpha,1}^x [V_{\alpha,1}] + F_{\alpha,2}^x [V_{\alpha,2}] + F_{\alpha,3}^x [V_{\alpha,3}] + F_{\alpha,4}^x [V_{\alpha,4}] + F_{\alpha,5}^x [V_{\alpha,5}] = [\psi_\alpha^x],$$

which simplifies to,

$$\begin{aligned} & \left(\frac{F_{\alpha,1}^x}{\rho_\alpha^{\text{ln}}} \right) [\rho_\alpha] + \left(\bar{\beta}_\alpha F_{\alpha,2}^x - \frac{\bar{\beta}_\alpha \bar{m}_{x_\alpha}}{\Gamma_\alpha} F_{\alpha,5}^x \right) [m_{x_\alpha}] + \left(\bar{\beta}_\alpha F_{\alpha,3}^x - \frac{\bar{\beta}_\alpha \bar{m}_{y_\alpha}}{\Gamma_\alpha} F_{\alpha,5}^x \right) [m_{y_\alpha}] \\ & + \left(\bar{\beta}_\alpha F_{\alpha,4}^x - \frac{\bar{\beta}_\alpha \bar{m}_{z_\alpha}}{\Gamma_\alpha} F_{\alpha,5}^x \right) [m_{z_\alpha}] + \left(k_\alpha F_{\alpha,1}^x + \bar{m}_{x_\alpha} F_{\alpha,2}^x + \bar{m}_{y_\alpha} F_{\alpha,3}^x + \bar{m}_{z_\alpha} F_{\alpha,4}^x - F_{\alpha,5}^x \Gamma_\alpha \right) [\beta_\alpha] \\ & = \bar{\rho}_\alpha [m_{x_\alpha}] + \bar{m}_{x_\alpha} [\rho_\alpha]. \end{aligned}$$

We want this equation to hold for all possible values of the jumps. This is possible if the coefficients of $[\rho_\alpha]$, $[\beta_\alpha]$, $[m_{x_\alpha}]$, $[m_{y_\alpha}]$, and $[m_{z_\alpha}]$, agree on both sides, which yields the following fluxes,

$$\tilde{\mathbf{F}}_{\alpha, i+\frac{1}{2}, j}^x = \tilde{\mathbf{F}}_\alpha^x(\mathbf{U}_{\alpha, i, j}, \mathbf{U}_{\alpha, i+1, j}) = \begin{pmatrix} \rho_\alpha^{\ln \overline{m_{x_\alpha}}} \\ \frac{1}{\beta_\alpha} \left(\frac{\overline{\beta_\alpha m_{x_\alpha}}}{\Gamma_\alpha} F_{\alpha, 5}^x + \overline{\rho_\alpha} \right) \\ \frac{\overline{m_{y_\alpha}}}{\Gamma_\alpha} F_{\alpha, 5}^x \\ \frac{\overline{m_{z_\alpha}}}{\Gamma_\alpha} F_{\alpha, 5}^x \\ -\overline{\Gamma_\alpha} \left(k_\alpha \rho_\alpha^{\ln \overline{m_{x_\alpha}}} + \frac{\overline{m_{x_\alpha} \rho_\alpha}}{\beta_\alpha} \right) \\ \frac{1}{(\overline{m_{x_\alpha}^2} + \overline{m_{y_\alpha}^2} + \overline{m_{z_\alpha}^2} - (\overline{\Gamma_\alpha})^2)} \end{pmatrix}_{i+\frac{1}{2}, j} \quad (31)$$

It is easy to verify that $\tilde{\mathbf{F}}_\alpha^x$ is consistent with the flux \mathbf{f}_α^x . Similarly, we can derive the expression for $\tilde{\mathbf{F}}_\alpha^y$ to get

$$\tilde{\mathbf{F}}_{\alpha, i, j+\frac{1}{2}}^y = \tilde{\mathbf{F}}_\alpha^y(\mathbf{U}_{\alpha, i, j}, \mathbf{U}_{\alpha, i, j+1}) = \begin{pmatrix} \rho_\alpha^{\ln \overline{m_{y_\alpha}}} \\ \frac{\overline{m_{x_\alpha}}}{\Gamma_\alpha} F_{\alpha, 5}^y \\ \frac{1}{\beta_\alpha} \left(\frac{\overline{\beta_\alpha m_{y_\alpha}}}{\Gamma_\alpha} F_{\alpha, 5}^y + \overline{\rho_\alpha} \right) \\ \frac{\overline{m_{z_\alpha}}}{\Gamma_\alpha} F_{\alpha, 5}^y \\ -\overline{\Gamma_\alpha} \left(k_\alpha \rho_\alpha^{\ln \overline{m_{y_\alpha}}} + \frac{\overline{m_{y_\alpha} \rho_\alpha}}{\beta_\alpha} \right) \\ \frac{1}{(\overline{m_{x_\alpha}^2} + \overline{m_{y_\alpha}^2} + \overline{m_{z_\alpha}^2} - (\overline{\Gamma_\alpha})^2)} \end{pmatrix}_{i, j+\frac{1}{2}}, \quad (32)$$

128 which is consistent with \mathbf{f}_α^y .

129 **Theorem 4.2.** *The numerical scheme (23), with the numerical fluxes (31) and (32) is second-order*
 130 *accurate and entropy conservative, i.e., it satisfy (24).*

131 *Proof.* Following [39] and [30], multiplying (23) with $\mathbf{V}_{\alpha, i, j}^\top$, we get,

$$\begin{aligned} \frac{d}{dt} \mathcal{U}_\alpha(\mathbf{U}_{\alpha, i, j}) + \frac{1}{\Delta x} \left(\tilde{\mathcal{F}}_{\alpha, i+\frac{1}{2}, j}^x - \tilde{\mathcal{F}}_{\alpha, i-\frac{1}{2}, j}^x \right) + \frac{1}{\Delta y} \left(\tilde{\mathcal{F}}_{\alpha, i, j+\frac{1}{2}}^y - \tilde{\mathcal{F}}_{\alpha, i, j-\frac{1}{2}}^y \right) \\ = \mathbf{V}_{\alpha, i, j}^\top \cdot \mathbf{s}_\alpha(\mathbf{U}_{\alpha, i, j}(t), \mathbf{U}_{m, i, j}(t)) \end{aligned}$$

Now, we note that

$$\mathbf{V}_{\alpha, i, j}^\top \cdot \mathbf{s}_\alpha(\mathbf{U}_{\alpha, i, j}(t), \mathbf{U}_{m, i, j}(t)) = 0$$

132 to arrive at the equality (24). □

The entropy conservative fluxes derived above are only second-order accurate. Following [41], we can use second-order fluxes to construct $2p^{th}$ -order accurate fluxes for any positive integer p . In particular, the 4^{th} -order ($p = 2$) x -directional entropy conservative flux $\tilde{\mathbf{F}}_{\alpha, i+\frac{1}{2}, j}^{x, 4}$ is given by,

$$\tilde{\mathbf{F}}_{\alpha, i+\frac{1}{2}, j}^{x, 4} = \frac{4}{3} \tilde{\mathbf{F}}_\alpha^x(\mathbf{U}_{\alpha, i, j}, \mathbf{U}_{\alpha, i+1, j}) - \frac{1}{6} \left(\tilde{\mathbf{F}}_\alpha^x(\mathbf{U}_{\alpha, i-1, j}, \mathbf{U}_{\alpha, i+1, j}) + \tilde{\mathbf{F}}_\alpha^x(\mathbf{U}_{\alpha, i, j}, \mathbf{U}_{\alpha, i+2, j}) \right).$$

133 Similarly, we can obtain the fourth-order entropy conservative flux $\tilde{\mathbf{F}}_{\alpha, i+\frac{1}{2}, j}^{y, 4}$ in y -direction. Combining
 134 this we have the following remarks.

135 **Remark 4.1.** *Replacing second-order fluxes with the higher-order fluxes in (23), we arrive at high-order,*
 136 *entropy conservative schemes.*

137 **Remark 4.2.** *The result from [41] gives only even order accurate fluxes. So, for q^{th} -order (q is an odd*
 138 *integer) accurate scheme, we use a $(q+1)^{th}$ -order (an even number) accurate flux.*

139 4.1.2 High-order entropy stable schemes for fluid equations

The entropy conservative schemes presented above will produce high-frequency oscillations near the shocks as they are central fluxes which do not dissipate entropy. Following [39], we introduce modified fluxes which will ensure entropy dissipation at the shocks. We consider a modified numerical flux of the form,

$$\begin{aligned} \mathbf{F}_{\alpha,i+\frac{1}{2},j}^x &= \tilde{\mathbf{F}}_{\alpha,i+\frac{1}{2},j}^x - \frac{1}{2} \mathbf{D}_{\alpha,i+\frac{1}{2},j}^x \llbracket \mathbf{V}_\alpha \rrbracket_{i+\frac{1}{2},j}, \\ \mathbf{F}_{\alpha,i,j+\frac{1}{2}}^y &= \tilde{\mathbf{F}}_{\alpha,i,j+\frac{1}{2}}^y - \frac{1}{2} \mathbf{D}_{\alpha,i,j+\frac{1}{2}}^y \llbracket \mathbf{V}_\alpha \rrbracket_{i,j+\frac{1}{2}}, \end{aligned} \quad (33)$$

140 where $\mathbf{D}_{\alpha,i+\frac{1}{2},j}^x$ and $\mathbf{D}_{\alpha,i,j+\frac{1}{2}}^y$ are symmetric positive definite matrices. Then we have the following
141 Lemma:

Lemma 4.1 (Tadmor [39]). *The numerical scheme (21) with the numerical fluxes (33) is entropy stable, i.e., the entropy inequality*

$$\frac{d}{dt} \mathcal{U}_\alpha(\mathbf{U}_{ij}) + \frac{1}{\Delta x} \left(\hat{\mathcal{F}}_{\alpha,i+\frac{1}{2},j}^x - \hat{\mathcal{F}}_{\alpha,i-\frac{1}{2},j}^x \right) + \frac{1}{\Delta y} \left(\hat{\mathcal{F}}_{\alpha,i,j+\frac{1}{2}}^y - \hat{\mathcal{F}}_{\alpha,i,j-\frac{1}{2}}^y \right) \leq 0, \quad \alpha \in \{i, e\},$$

is satisfied with the consistent numerical entropy flux functions,

$$\begin{aligned} \hat{\mathcal{F}}_{\alpha,i+\frac{1}{2},j}^x &= \tilde{\mathcal{F}}_{\alpha,i+\frac{1}{2},j}^x + \frac{1}{2} (\bar{\mathbf{V}}_\alpha)_{i+\frac{1}{2},j}^\top \mathbf{D}_{\alpha,i+\frac{1}{2},j}^x \llbracket \mathbf{V}_\alpha \rrbracket_{i+\frac{1}{2},j}, \\ \hat{\mathcal{F}}_{\alpha,i,j+\frac{1}{2}}^y &= \tilde{\mathcal{F}}_{\alpha,i,j+\frac{1}{2}}^y + \frac{1}{2} (\bar{\mathbf{V}}_\alpha)_{i,j+\frac{1}{2}}^\top \mathbf{D}_{\alpha,i,j+\frac{1}{2}}^y \llbracket \mathbf{V}_\alpha \rrbracket_{i,j+\frac{1}{2}}. \end{aligned}$$

We will use *Rusanov type* diffusion operators for the matrix \mathbf{D}_α , which is given by,

$$\mathbf{D}_{\alpha,i+\frac{1}{2},j}^x = \tilde{\mathbf{R}}_{\alpha,i+\frac{1}{2},j}^x \Lambda_{\alpha,i+\frac{1}{2},j}^x \tilde{\mathbf{R}}_{\alpha,i+\frac{1}{2},j}^{x\top}, \quad \text{and} \quad \mathbf{D}_{\alpha,i,j+\frac{1}{2}}^y = \tilde{\mathbf{R}}_{\alpha,i,j+\frac{1}{2}}^y \Lambda_{\alpha,i,j+\frac{1}{2}}^y \tilde{\mathbf{R}}_{\alpha,i,j+\frac{1}{2}}^{y\top}. \quad (34)$$

where $\tilde{\mathbf{R}}_\alpha^d$, $d \in \{x, y\}$, are matrices of the entropy scaled right eigenvectors and Λ_α^d are 5×5 diagonal matrices of the form

$$\Lambda_\alpha^d = \left(\max_{1 \leq k \leq 5} |\Lambda_{\alpha_k}^d| \right) \mathbf{I}_{5 \times 5},$$

where $\{\Lambda_{\alpha_k}^d : 1 \leq k \leq 5\}$, $d \in \{x, y\}$, are the eigenvalues. Following [42], we have $\partial_{\mathbf{V}_\alpha} \mathbf{U}_\alpha = \tilde{\mathbf{R}}_\alpha^d (\tilde{\mathbf{R}}_\alpha^d)^\top$ for $d \in \{x, y\}$, hence,

$$\tilde{\mathbf{R}}_\alpha^d \Lambda_\alpha^d (\tilde{\mathbf{R}}_\alpha^d)^{(-1)} \llbracket \mathbf{U}_\alpha \rrbracket \approx \tilde{\mathbf{R}}_\alpha^d \Lambda_\alpha^d (\tilde{\mathbf{R}}_\alpha^d)^{(-1)} \partial_{\mathbf{V}_\alpha} \mathbf{U}_\alpha \llbracket \mathbf{V}_\alpha \rrbracket = \tilde{\mathbf{R}}_\alpha^d \Lambda_\alpha^d (\tilde{\mathbf{R}}_\alpha^d)^\top \llbracket \mathbf{V}_\alpha \rrbracket,$$

142 i.e., the entropy diffusion operator used here is similar to the *Roe* diffusion operator when the entropy
143 scaled right eigenvectors are used. The complete expressions for $\tilde{\mathbf{R}}_\alpha^d$ are derived in Appendix (A.2).

With the choice of diffusion operator (34), the numerical scheme (21) with the numerical flux (33) is entropy stable. However, the scheme is only first-order accurate due to the presence of the first-order jump terms $\llbracket \mathbf{V}_\alpha \rrbracket_{i+\frac{1}{2},j}$ and $\llbracket \mathbf{V}_\alpha \rrbracket_{i,j+\frac{1}{2}}$. A straightforward way to increase the order of accuracy is to approximate the jumps in the diffusive term of (33) using a higher-order reconstruction process. However, proving the entropy stability of the resulting scheme is not possible. Instead, we follow the process prescribed in [30] and introduce the *scaled entropy variables*. We illustrate the procedure for the x -direction only, as the y -directional case is similar. Define the change of variables

$$\mathcal{V}_{\alpha,m,j}^{x,\pm} = (\tilde{\mathbf{R}}_{\alpha,i\pm\frac{1}{2},j}^x)^\top \mathbf{V}_{\alpha,m,j}, \quad m \text{ are neighbours of cell } (i, j) \text{ along } x$$

Using ENO procedure we choose a stencil of cells and construct the polynomials $P_{i,j}^{x,\pm}(x)$ of degree k and evaluate it at the faces of cell (i, j)

$$\tilde{\mathcal{V}}_{\alpha,i,j}^{x,\pm} = P_{i,j}^{x,\pm}(x_{i\pm\frac{1}{2}})$$

Converting back to the entropy variables,

$$\tilde{\mathbf{V}}_{\alpha,i,j}^{x,\pm} = \left\{ (\tilde{\mathbf{R}}_{\alpha,i\pm\frac{1}{2},j}^x)^\top \right\}^{(-1)} \mathcal{V}_{\alpha,i,j}^{x,\pm}$$

are the corresponding k -th order reconstructed values for \mathbf{V}_α . Hence the high-order entropy stable numerical flux is given by,

$$\mathbf{F}_{\alpha, i+\frac{1}{2}, j}^{x, k} = \tilde{\mathbf{F}}_{\alpha, i+\frac{1}{2}, j}^{x, 2p} - \frac{1}{2} \mathbf{D}_{\alpha, i+\frac{1}{2}, j}^x \llbracket \tilde{\mathbf{V}}_\alpha^x \rrbracket_{i+\frac{1}{2}, j} \quad (35)$$

where $\llbracket \tilde{\mathbf{V}}_\alpha^x \rrbracket_{i+\frac{1}{2}, j}$ stands for,

$$\llbracket \tilde{\mathbf{V}}_\alpha^x \rrbracket_{i+\frac{1}{2}, j} = \tilde{\mathbf{V}}_{\alpha, i+1, j}^{x, -} - \tilde{\mathbf{V}}_{\alpha, i, j}^{x, +}.$$

144 As only even order entropy conservative fluxes $\tilde{\mathbf{F}}_{\alpha, i+\frac{1}{2}, j}^{x, 2p}$ are available and we choose $p \in \mathbb{N}$ as

145 • $p = k/2$ if k is even,

146 • $p = (k+1)/2$ if k is odd,

147 where k is the order of the scheme. Following [30], a sufficient condition for the numerical flux (35)
148 to be entropy stable is that the reconstruction process for \mathcal{V} must satisfy the *sign preserving property*.
149 For the second-order reconstruction, we use the *min-mod* reconstruction, which satisfies this property.
150 Following [31], we use ENO reconstruction as it satisfies the *sign preserving property*. For third and
151 fourth-order schemes, we use fourth-order entropy conservative flux along with the third and fourth-
152 order ENO reconstruction of the scaled entropy variables. We now have the following result:

153 **Theorem 4.3.** *The numerical scheme (23) with entropy stable flux (35) satisfies the entropy inequality*
154 *(25).*

Proof. The proof follows from [30] and the fact that,

$$\mathbf{V}_{\alpha, i, j}^\top \cdot \mathbf{s}_\alpha(\mathbf{U}_{\alpha, i, j}(t), \mathbf{U}_{m, i, j}(t)) = 0$$

155

□

156 **Remark 4.3.** *The above result holds for any discretization of Maxwell's equations.*

157 4.2 Discretization of Maxwell's equations

To spatially discretize the Maxwell's equations (1g)-(1j), we use the finite-difference scheme based on the Rusanov solver. The x - and y -directional numerical fluxes are given by

$$\begin{aligned} \mathbf{F}_{m, i+\frac{1}{2}, j}^x &= \frac{1}{2} (\mathbf{f}_m^x(\mathbf{U}_{m, i, j}) + \mathbf{f}_m^x(\mathbf{U}_{m, i+1, j})) - \frac{c}{2} (\mathbf{U}_{m, i+1, j} - \mathbf{U}_{m, i, j}), \\ \mathbf{F}_{m, i, j+\frac{1}{2}}^y &= \frac{1}{2} (\mathbf{f}_m^y(\mathbf{U}_{m, i, j}) + \mathbf{f}_m^y(\mathbf{U}_{m, i, j+1})) - \frac{c}{2} (\mathbf{U}_{m, i, j+1} - \mathbf{U}_{m, i, j}). \end{aligned}$$

158 where $c = 1$ is the speed of light. To obtain higher accuracy, we use *min-mod* limiter [25] to reconstruct
159 the variables \mathbf{U}_m at the cell faces to get the second-order scheme. Furthermore, we use third and
160 fifth-order WENO reconstructions [43] to obtain the third- and fourth-order Rusanov's solver for the
161 Maxwell's equations.

162 5 Fully discrete scheme

Let \mathbf{U}^n be the discrete solution at time t^n , where the time step is $\Delta t = t^{n+1} - t^n$. The semi-discrete scheme (21) can be expressed as

$$\frac{d}{dt} \mathbf{U}_{i, j}(t) = \mathcal{L}_{i, j}(\mathbf{U}(t)) + \mathbf{s}(\mathbf{U}_{i, j}(t)), \quad \mathbf{U}_{i, j}(t^n) = \mathbf{U}^n \quad (37)$$

where,

$$\mathcal{L}_{i, j}(\mathbf{U}(t)) = -\frac{1}{\Delta x} \left(\mathbf{F}_{i+\frac{1}{2}, j}^x(t) - \mathbf{F}_{i-\frac{1}{2}, j}^x(t) \right) - \frac{1}{\Delta y} \left(\mathbf{F}_{i, j+\frac{1}{2}}^y(t) - \mathbf{F}_{i, j-\frac{1}{2}}^y(t) \right).$$

163 We propose fully explicit and IMEX schemes for the above system.

5.1 Explicit schemes

For the explicit time discretizations, we use explicit strong stability preserving Runge Kutta (SSP-RK) methods [44]. The second and third-order accurate SSP-RK schemes are given as follows.

1. Set $\mathbf{U}^0 = \mathbf{U}^n$.
2. For $m = 1, \dots, k + 1$, compute,

$$\mathbf{U}_{i,j}^{(m)} = \sum_{l=0}^{m-1} \alpha_{ml} \mathbf{U}_{i,j}^{(l)} + \beta_{ml} \Delta t (\mathcal{L}_{i,j}(\mathbf{U}^{(l)}) + \mathbf{s}(\mathbf{U}_{i,j}^{(l)})),$$

where, α_{ml} and β_{ml} follows from the Table (1).

3. Finally, $\mathbf{U}_{i,j}^{n+1} = \mathbf{U}_{i,j}^{(k+1)}$.

Order	α_{il}			β_{il}		
2	1			1		
	1/2	1/2		0	1/2	
3	1			1		
	3/4	1/4		0	1/4	
	1/3	0	2/3	0	0	2/3

Table 1: Coefficients for SSP Runge-Kutta time stepping

The fourth order RK-SSP is given by,

$$\begin{aligned} \mathbf{U}_{i,j}^{(1)} &= \mathbf{U}_{i,j}^n + 0.39175222700392 (\Delta t) (\mathcal{L}_{i,j}(\mathbf{U}^n) + \mathbf{s}(\mathbf{U}_{i,j}^n)), \\ \mathbf{U}_{i,j}^{(2)} &= 0.44437049406734 \mathbf{U}_{i,j}^n + 0.55562950593266 \mathbf{U}_{i,j}^{(1)} \\ &\quad + 0.36841059262959 (\Delta t) (\mathcal{L}_{i,j}(\mathbf{U}^{(1)}) + \mathbf{s}(\mathbf{U}_{i,j}^{(1)})), \\ \mathbf{U}_{i,j}^{(3)} &= 0.62010185138540 \mathbf{U}_{i,j}^n + 0.37989814861460 \mathbf{U}_{i,j}^{(2)} \\ &\quad + 0.25189177424738 (\Delta t) (\mathcal{L}_{i,j}(\mathbf{U}^{(2)}) + \mathbf{s}(\mathbf{U}_{i,j}^{(2)})), \\ \mathbf{U}_{i,j}^{(4)} &= 0.17807995410773 \mathbf{U}_{i,j}^n + 0.82192004589227 \mathbf{U}_{i,j}^{(3)} \\ &\quad + 0.54497475021237 (\Delta t) (\mathcal{L}_{i,j}(\mathbf{U}^{(3)}) + \mathbf{s}(\mathbf{U}_{i,j}^{(3)})), \\ \mathbf{U}_{i,j}^{n+1} &= 0.00683325884039 \mathbf{U}^n + 0.51723167208978 \mathbf{U}_{i,j}^{(2)} + 0.12759831133288 \mathbf{U}_{i,j}^{(3)} \\ &\quad + 0.34833675773694 \mathbf{U}_{i,j}^{(4)} + 0.08460416338212 (\Delta t) (\mathcal{L}_{i,j}(\mathbf{U}^{(3)}) + \mathbf{s}(\mathbf{U}_{i,j}^{(3)})) \\ &\quad + 0.22600748319395 (\Delta t) (\mathcal{L}_{i,j}(\mathbf{U}^{(4)}) + \mathbf{s}(\mathbf{U}_{i,j}^{(4)})). \end{aligned}$$

We use a second-order spatial accurate scheme with a second-order explicit time scheme, which is denoted by, **O2-ES-Exp**. Similarly, the third-order spatial accurate scheme is time-discretized with the third-order RK method above and denoted by, **O3-ES-Exp**. The fourth-order scheme consists of fourth-order spatial discretization with the fourth-order time update above and denoted by **O4-ES-Exp**.

5.2 ARK-IMEX schemes

In several cases, the values of charge to mass ratios r_α can be very large. In those cases, the source terms will be stiff. This will result in a time-step restriction when using the explicit scheme discussed above. To overcome this difficulty, we propose Additive Runge Kutta Implicit Explicit (ARK IMEX) time updates from [45]. Here, the flux terms will be treated explicitly, and the source terms will be treated implicitly. We write the semi-discrete scheme (21) in a simplified form as follows

$$\frac{\partial \mathbf{U}}{\partial t} = F_{NS}(\mathbf{U}(t)) + F_S(\mathbf{U}(t)),$$

where $F_{NS}(\mathbf{U}(t)) = \mathcal{L}_{i,j}(\mathbf{U}(t))$ denotes the non-stiff flux terms, and $F_S(\mathbf{U}(t)) = \mathbf{s}(\mathbf{U}_{i,j}(t))$ denotes the stiff source terms. Note that the source terms depend only on the solution value in the parent cell and do not depend on the solutions in neighboring cells.

5.2.1 Second order time discretization.

For the second-order discretization, we use L-Stable second-order accurate ARK IMEX scheme from [45]. The method has two implicit stages and is given by

$$\begin{aligned}\mathbf{U}^{(1)} &= \mathbf{U}^n + \Delta t (\beta F_S(\mathbf{U}^{(1)}(t^n))), \\ \mathbf{U}^{(2)} &= \mathbf{U}^n + \Delta t (F_{NS}(\mathbf{U}^{(1)}(t^n)) + (1 - 2\beta)F_S(\mathbf{U}^{(1)}(t^n)) + \beta F_S(\mathbf{U}^{(2)}(t^n))), \\ \mathbf{U}^{(n+1)} &= \mathbf{U}^n + \Delta t \left(\frac{1}{2}F_{NS}(\mathbf{U}^{(1)}(t^n)) + \frac{1}{2}F_{NS}(\mathbf{U}^{(2)}(t^n)) + \frac{1}{2}F_S(\mathbf{U}^{(1)}(t^n)) + \frac{1}{2}F_S(\mathbf{U}^{(2)}(t^n)) \right),\end{aligned}$$

where $\beta = 1 - \frac{1}{\sqrt{2}}$. Note that, to evaluate \mathbf{U}^1 and \mathbf{U}^2 , we need to solve a nonlinear system of algebraic equations. However, the resulting equations are only local, i.e., we get an independent set of equations for each cell. We solve these equations using the Newton's method, where the convergence and the next direction search is based on the backtracing line search framework. A detailed procedure is given in [46]. In the higher-order method, we will use the same process to update the internal IMEX steps.

5.2.2 Third and fourth-order time discretization.

For the higher-order discretization, we use L-Stable ARK IMEX methods from [47]. We ignore the subscripts $\{i, j\}$ for simplicity. The ARK scheme from [47] has the following steps.

1. Set $\mathbf{U}^0 = \mathbf{U}^n$.
2. For $m = 1, \dots, k$, compute,

$$\mathbf{U}^{(m)} = \mathbf{U}^n + \Delta t \sum_{l=0}^{m-1} a_{ml}^{[NS]} F_{NS}(\mathbf{U}^l) + \Delta t \sum_{l=0}^m a_{ml}^{[S]} F_S(\mathbf{U}^l),$$

where, $\mathbf{U}^{(m)}$ approximates $\mathbf{U}(t^n + c_m \Delta t)$.

3. Finally,

$$\mathbf{U}^{n+1} = \mathbf{U}^n + \Delta t \sum_{l=0}^k b_l^{[NS]} F_{NS}(\mathbf{U}^l) + \Delta t \sum_{l=0}^k b_l^{[S]} F_S(\mathbf{U}^l),$$

where k is the order of the desired time discretization (k ranges from 3 to 5), and coefficients $a_{ml}^{[NS]}$, $a_{ml}^{[S]}$, $b_l^{[NS]}$, $b_l^{[S]}$, c_l are defined accordingly by the order of accuracy and stability considerations.

We present coefficients for the third-order scheme in Appendix (B). The coefficients for the fourth-order time update can be found in [47]. We denote the second-order IMEX scheme with **O2-ES-IMEX**, third-order IMEX scheme with **O3-ES-IMEX** and fourth-order IMEX scheme with **O4-ES-IMEX**.

6 Numerical results

In this section, we present numerical results for various test cases. We set specific heat constants $\gamma_i = \gamma_e = 4/3$, unless stated otherwise. In some test cases, we need to consider the resistive effects. To take them into consideration, following [12], we modify the momentum ((1e),(1b)) and energy equations ((1c),(1f)) for the fluid parts by adding resistive terms as follows,

$$\frac{\partial(\rho_\alpha h_\alpha \Gamma_\alpha^2 \mathbf{u}_\alpha)}{\partial t} + \nabla \cdot (\rho_\alpha h_\alpha \Gamma_\alpha^2 \mathbf{u}_\alpha \mathbf{u}_\alpha^\top + p_\alpha \mathbf{I}) = r_\alpha \Gamma_\alpha \rho_\alpha (\mathbf{E} + \mathbf{u}_\alpha \times \mathbf{B}) + \mathbf{R}_\alpha, \quad (40a)$$

$$\frac{\partial(\mathcal{E}_\alpha)}{\partial t} + \nabla \cdot ((\mathcal{E}_\alpha + p_\alpha) \mathbf{u}_\alpha) = r_\alpha \Gamma_\alpha \rho_\alpha (\mathbf{u}_\alpha \cdot \mathbf{E}) + R_\alpha^0, \quad (40b)$$

for $\alpha \in \{i, e\}$. Following [12], an anti-symmetry relationship, $(\mathbf{R}_e, R_e^0) = (-\mathbf{R}_i, -R_i^0)$, has been assumed for the conservation of the total momentum and energy density. The expressions for the terms \mathbf{R}_i and R_i^0 are given by

$$\mathbf{R}_i = -\eta \frac{\omega_p^2}{r_i - r_e} (\mathbf{j} - \rho_0 \Phi), \quad R_i^0 = -\eta \frac{\omega_p^2}{r_i - r_e} (\rho_c - \rho_0 \Lambda),$$

where,

$$\begin{aligned} \omega_p^2 &= r_i^2 \rho_i + r_e^2 \rho_e, & \Phi &= \frac{r_i \rho_i \Gamma_i \mathbf{u}_i + r_e \rho_e \Gamma_e \mathbf{u}_e}{\omega_p^2}, \\ \Lambda &= \frac{r_i^2 \rho_i \Gamma_i + r_e^2 \rho_e \Gamma_e}{\omega_p^2}, & \rho_0 &= \Lambda \rho_c - \mathbf{j} \cdot \Phi \end{aligned} \quad (41)$$

and η is the resistivity constant. Here, ω_p is the total plasma frequency. The total plasma skin depth d_p is defined as $d_p = \frac{1}{\omega_p}$. For the time update using ARK IMEX scheme, we couple the resistive terms with the other source terms and treat them implicitly, i.e., we modify F_S to include the resistive terms.

To compare the numerical results with published work consistently, for all the test cases taken from [29], we multiply the source term for Maxwell's equations by 4π , i.e., we consider,

$$\mathbf{s}_m = 4\pi \begin{pmatrix} 0 \\ 0 \\ 0 \\ -j_x \\ -j_y \\ -j_z \end{pmatrix}. \quad (42)$$

Consequently, in the test cases from [29], the total plasma skin depth is given by $d_p = \frac{\sqrt{2}}{\omega_p}$ with $\omega_p^2 = 4\pi(r_i^2 \rho_i + r_e^2 \rho_e)$.

6.1 One-dimensional test cases

For the one-dimensional test cases, the time step is chosen using

$$\Delta t = \text{CFL} \cdot \min \left\{ \frac{\Delta x}{\Lambda_{max}^x(\mathbf{U}_i)} : 1 \leq i \leq N_x \right\}, \text{ where } \Lambda_{max}^x(\mathbf{U}_i) = \max\{|\Lambda_k^x(\mathbf{U}_i)| : 1 \leq k \leq 16\}.$$

We take CFL to be 0.8, for the explicit (**O2-ES-Exp**, **O3-ES-Exp** and **O4-ES-Exp**), and ARK IMEX schemes (**O2-ES-IMEX**, **O3-ES-IMEX** and **O4-ES-IMEX**), unless stated otherwise.

6.1.1 Accuracy test

Number of cells	O2-ES-Exp		O3-ES-Exp		O4-ES-Exp	
—	L^1 error	Order	L^1 error	Order	L^1 error	Order
50	4.65354e-02	—	1.45685e-03	—	3.72752e-05	—
100	1.46178e-02	1.6706	2.10073e-04	2.7939	2.83586e-06	3.7164
200	4.06539e-03	1.8463	2.68670e-05	2.9670	2.00245e-07	3.8239
400	1.10156e-03	1.8838	3.38951e-06	2.9867	1.38798e-08	3.8507
800	2.96426e-04	1.8938	4.12557e-07	3.0384	9.36376e-10	3.8898
1600	7.83484e-05	1.9197	4.74611e-08	3.1198	6.20992e-11	3.9144
3200	2.04441e-05	1.9382	5.12937e-09	3.2099	4.42086e-12	3.8122

Table 2: **Accuracy test**: L^1 errors and order of convergence for ρ_i using the explicit entropy stable schemes **O2-ES-Exp**, **O3-ES-Exp** and **O4-ES-Exp**.

Number of cells	O2-ES-IMEX		O3-ES-IMEX		O4-ES-IMEX	
–	L^1 error	Order	L^1 error	Order	L^1 error	Order
50	4.61786e-02	–	1.47485e-03	–	1.49887e-04	–
100	1.44393e-02	1.6772	2.11249e-04	2.8036	1.13242e-05	3.7264
200	4.00815e-03	1.8490	2.70271e-05	2.9665	7.99400e-07	3.8243
400	1.09588e-03	1.8708	3.40274e-06	2.9896	5.54233e-08	3.8504
800	2.94580e-04	1.8954	4.13678e-07	3.0401	3.73687e-09	3.8906
1600	7.77739e-05	1.9213	4.75938e-08	3.1197	2.47401e-10	3.9169
3200	2.02876e-05	1.9387	5.14414e-09	3.2098	1.63538e-11	3.9192

Table 3: **Accuracy test**: L^1 errors and order of convergence for ρ_i using the ARK IMEX entropy stable schemes **O2-ES-IMEX**, **O3-ES-IMEX** and **O4-ES-IMEX**.

To test the accuracy and order of convergence of the proposed scheme, we consider a test case with smooth solution. We follow a forced solution approach of [15] to modify the smooth test case from [1]. We add forcing term $\mathcal{S}(x, t)$ to write the one-dimensional modified system (4) as

$$\frac{\partial \mathbf{U}}{\partial t} + \frac{\partial \mathbf{f}^x}{\partial x} = \mathbf{s} + \mathcal{S}(x, t)$$

with

$$\mathcal{S}(x, t) = \left(\mathbf{0}_{13}, -\frac{1}{\sqrt{3}}(2 + \sin(2\pi(x - 0.5t))), 0, -3\pi \cos(2\pi(x - 0.5t)) \right)^\top.$$

We set initial ion and electron densities as $\rho_i = \rho_e = 2 + \sin(2\pi x)$, with initial velocities $u_{x_i} = u_{x_e} = 0.5$ and initial pressures $p_i = p_e = 1$. The y -magnetic component is $B_y = 2 \sin(2\pi(x))$ and the z -electric field component is $E_z = -\sin(2\pi(x))$. All other primitive variables are set to zero. We use computational domain $I = [0, 1]$ with the periodic boundary conditions. We also set charge to mass ratios $r_i = 1$ and $r_e = -2$, consequently we have non-zero electric field source term \mathbf{j} . For the present test, we use ion-electron adiabatic index $\gamma = 5/3$. Using the above conditions, it is easy to verify that the exact solution is $\rho_i = \rho_e = 2 + \sin(2\pi(x - 0.5t))$.

In Table (2) and Table (3), we have presented the results for explicit (**O2-ES-Exp**, **O3-ES-Exp** and **O4-ES-Exp**) and ARK-IMEX schemes (**O2-ES-IMEX**, **O3-ES-IMEX**, and **O4-ES-IMEX**) at the final time $t = 2.0$. We have presented L^1 -errors for ρ_i at different resolutions. For both explicit and IMEX schemes, we observe a consistent order of accuracy at various resolutions. Furthermore, we also note that the errors for both explicit and IMEX schemes of same order are comparable at a given resolution.

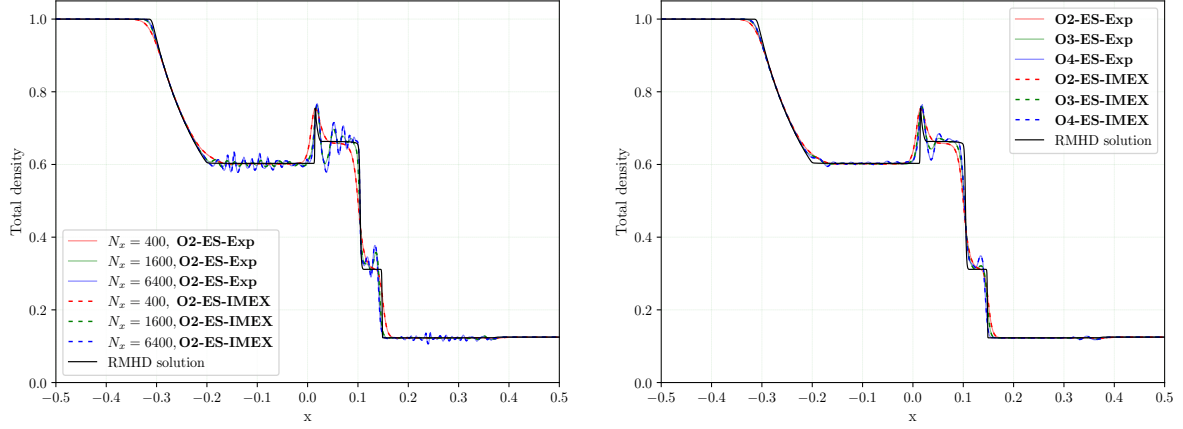
6.1.2 Relativistic Brio–Wu test problem with finite plasma skin depth

In this test case, we consider one-dimensional Brio-Wu shock tube problem with finite plasma skin depth from [12, 29]. This problem is a two-fluid extension of the relativistic analogue of the Brio-Wu shock tube problem given in [7]. In this case, we consider the Maxwell’s source (42), and no resistive effects are considered. We take the computational domain to be $[-0.5, 0.5]$ with Neumann boundary conditions at both boundaries. The initial discontinuity is assumed to be placed at $x = 0.0$. Following [29], the initial Riemann data is given by,

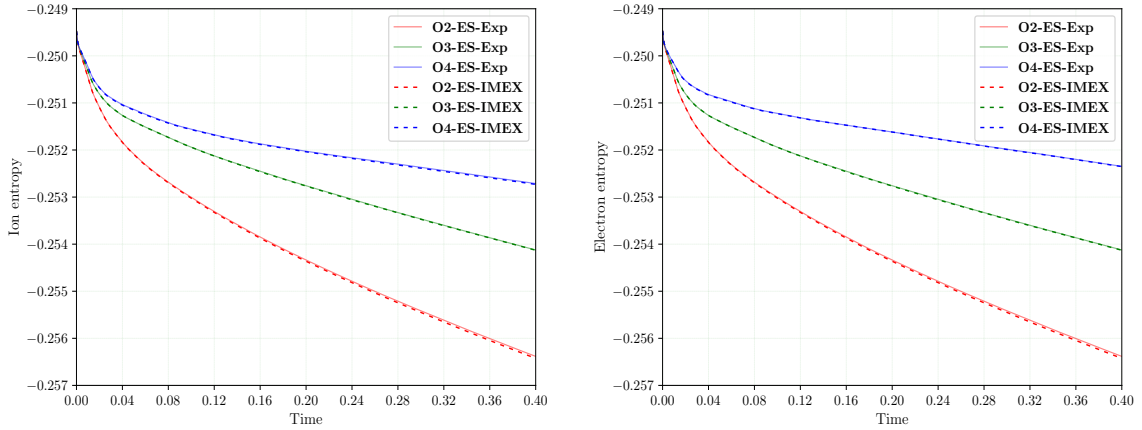
$$\mathbf{W}_L = \begin{pmatrix} \rho_i \\ p_i \\ \rho_e \\ p_e \\ B_x \\ B_y \end{pmatrix}_L = \begin{pmatrix} 0.5 \\ 0.5 \\ 0.5 \\ 0.5 \\ \sqrt{\pi} \\ \sqrt{4\pi} \end{pmatrix}, \quad \mathbf{W}_R = \begin{pmatrix} \rho_i \\ p_i \\ \rho_e \\ p_e \\ B_x \\ B_y \end{pmatrix}_R = \begin{pmatrix} 0.0625 \\ 0.05 \\ 0.0625 \\ 0.05 \\ \sqrt{\pi} \\ -\sqrt{4\pi} \end{pmatrix}.$$

All other variables are set to zero. Following [29], the specific heat ratios are set to $\gamma_i = \gamma_e = 2.0$, and we compute the solution till final time $t = 0.4$.

First, we consider charge to mass ratios as $r_i = -r_e = 10^3/\sqrt{4\pi}$, thus the plasma skin depth is $10^{-3}/\sqrt{\rho_i}$. Consequently, we expect solutions to be close to the RMHD results whenever the resolution of the cells is larger than the plasma skin depth.



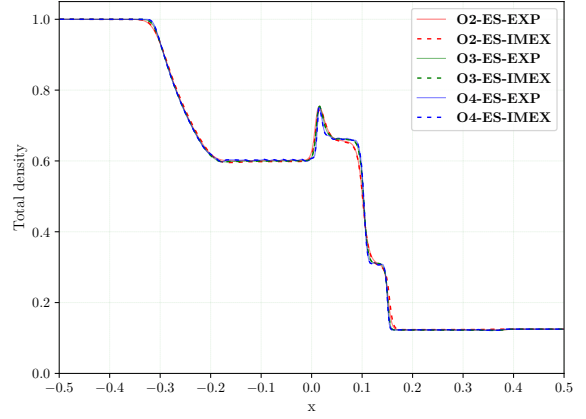
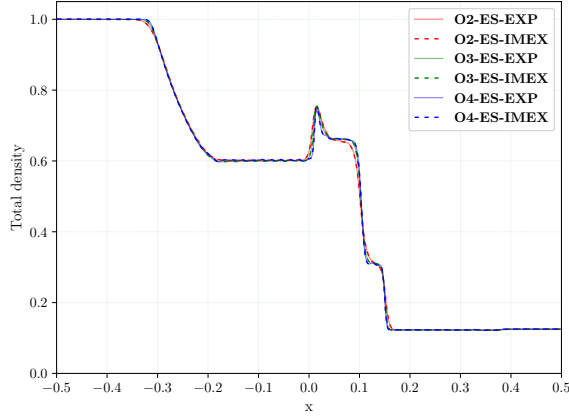
(a) Plots of total density $\rho_i + \rho_e$ for second-order schemes (**O2-ES-Exp** and **O2-ES-IMEX**) using 400, 1600 and 6400 cells. (b) Plots of total density $\rho_i + \rho_e$, for second (**O2-ES-Exp** and **O2-ES-IMEX**), third (**O3-ES-Exp** and **O3-ES-IMEX**), and fourth (**O4-ES-Exp** and **O4-ES-IMEX**) order schemes using 400 cells.



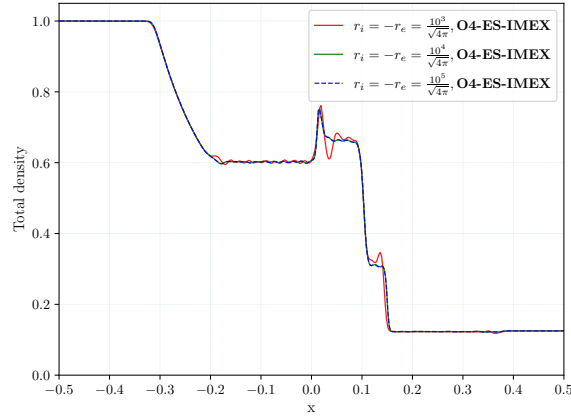
(c) Plots of total ion entropy for second (**O2-ES-Exp** and **O2-ES-IMEX**), third (**O3-ES-Exp** and **O3-ES-IMEX**), and fourth (**O4-ES-Exp** and **O4-ES-IMEX**) order schemes using 400 cells. (d) Plots of total electron entropy for second (**O2-ES-Exp** and **O2-ES-IMEX**), third (**O3-ES-Exp** and **O3-ES-IMEX**), and fourth (**O4-ES-Exp** and **O4-ES-IMEX**) order schemes using 400 cells.

Figure 1: Numerical results for **Relativistic Brio–Wu test problem with finite plasma skin depth** using different schemes and grid resolutions.

To compare with the results of [29], in Figure 1(a), we plot the total density $\rho_i + \rho_e$ for **O2-ES-Exp** and **O2-ES-IMEX** schemes using 400, 1600 and 6400 cells. To compare the solution with RMHD solution, we have computed “RMHD” solution using $r_i = -r_e = 10^5/\sqrt{4\pi}$ at 6400 cells and **O2-ES-IMEX** scheme. We observe that on a resolution of 400 cells, the cell size $\Delta x = 0.0025$ is slightly larger than the plasma skin depth in the entire domain; thus, the profile roughly matches with the RMHD results [7], while at the higher resolutions, 1600 and 6400, the cell size is much smaller than the plasma skin depth, consequently, appearance of the two-fluid effect in the form of dispersive waves is observed. We also note that both explicit (**O2-ES-Exp**) and IMEX (**O2-ES-IMEX**) schemes have similar performance in capturing all the waves and additional effects at the various resolutions.



(a) Plots of total density $\rho_i + \rho_e$, for second (**O2-ES-Exp** and **O2-ES-IMEX**), third (**O3-ES-Exp** and **O3-ES-IMEX**), and fourth (**O4-ES-Exp** and **O4-ES-IMEX**) order schemes with $r_i = -r_e = 10^4/\sqrt{4\pi}$ using **IMEX** order schemes with $r_i = -r_e = 10^5/\sqrt{4\pi}$ using 400 cells.



(c) Plots of total density $\rho_i + \rho_e$, for **O4-ES-IMEX** scheme for various stiff cases at 400 cells.

Figure 2: Numerical results for **Relativistic Brio–Wu test problem with finite plasma skin depth** using various stiff cases at 400 cells.

To compare second-order schemes, with the third and fourth-order schemes, in Figure (1(b)), we have plotted total density for explicit (**O2-ES-Exp**, **O3-ES-Exp** and **O4-ES-Exp**) and ARK-IMEX schemes (**O2-ES-IMEX**, **O3-ES-IMEX**, and **O4-ES-IMEX**) at 400 cells. We observe that the third and fourth-order schemes are able to capture the additional dispersive effects even on the coarser mesh. We also note that fourth-order schemes are more effective in capturing these effects compared to the third-order scheme. Furthermore, both third-order schemes (**O3-ES-Exp** and **O3-ES-IMEX**) have similar performance. Similarly, both fourth-order schemes (**O4-ES-Exp** and **O4-ES-IMEX**) have similar performance.

We can also observe this from the time evolution of total entropy plots for ion flow in Figure (1(c)) and electron flow in Figure (1(d)). We note that the same order schemes have almost the same entropy decay behaviour. Furthermore, third and fourth-order schemes decay less entropy compared to the second-order schemes. Similarly, fourth-order schemes are less entropy decaying than the third-order schemes.

	$r_i = -r_e = 10^4/\sqrt{4\pi}$				$r_i = -r_e = 10^5/\sqrt{4\pi}$			
Number of cells	100	200	400	800	100	200	400	800
O2-ES-Exp	3.31s	6.0s	11.04s	20.81s	76.99s	157.17s	288.66s	506.90s
O2-ES-IMEX	0.45s	1.06s	4.17s	11.27s	0.61s	1.41s	4.40s	15.51s
O3-ES-Exp	2.19s	4.34s	7.90s	13.62s	29.86s	54.09s	98.92s	190.71s
O3-ES-IMEX	0.86s	2.64s	6.57s	24.79s	1.13s	2.67s	6.59s	25.13s
O4-ES-Exp	5.84s	10.02s	18.03s	34.61s	56.53s	102.79s	198.36s	359.40s
O4-ES-IMEX	1.28s	3.85s	13.96s	54.91s	1.32s	4.23s	14.31s	49.10s

Table 4: **Relativistic Brio–Wu test problem with finite plasma skin depth**: Computational times using $r_i = -r_e = 10^4/\sqrt{4\pi}$ and $r_i = -r_e = 10^5/\sqrt{4\pi}$ for the second (**O2-ES-Exp** and **O2-ES-IMEX**), third (**O3-ES-Exp** and **O3-ES-IMEX**), and fourth (**O4-ES-Exp** and **O4-ES-IMEX**) order schemes.

We also consider the stiff source terms with $r_i = -r_e = 10^4/\sqrt{4\pi}$ and $r_i = -r_e = 10^5/\sqrt{4\pi}$. We remark that in this case plasma skin depth is very small, hence we do not expect any scheme to resolve the dispersive effects and we will need substantial more number of cells to resolve them. In Figure (2), we have plotted solutions for different schemes using 400 cells. We note that for both the value of r_i , all the schemes produce solutions close to RMHD solution, with third and fourth-order schemes performing better than the second-order schemes. Also, there is no visible difference in Explicit and IMEX scheme of same order. To further show the effects of higher values of r_i , in Figure (2(c)), we have plotted solutions using **O4-ES-IMEX** scheme on 400 cells, for different values of r_i . For $r_i = 10^3/\sqrt{4\pi}$, we can see the dispersive effects are resolved. However, for $r_i = 10^4/\sqrt{4\pi}$ and $r_i = 10^5/\sqrt{4\pi}$, scheme was not able to resolve the small scale oscillation; nevertheless, the scheme produce a stable solution thanks to the built in entropy stability property of the scheme.

To demonstrate the effectiveness of ARK-IMEX schemes over the explicit schemes for the stiff source terms, in Table (4), we present the computational time for the cases $r_i = -r_e = 10^4/\sqrt{4\pi}$ and $r_i = -r_e = 10^5/\sqrt{4\pi}$ on 100, 200, 400, and 800 cells. We use the MPI-parallelized code on 10 cores. At the lower resolutions, the source terms will govern the time step as time step given by the CFL restriction is large. Hence, we observe consistently that IMEX schemes outperform the explicit schemes on the coarser mesh. In the case of $r_i = -r_e = 10^4/\sqrt{4\pi}$, we see that IMEX outperform the explicit schemes up to 400 cells. On 800 cells, we observe that the IMEX schemes are more expensive than the explicit schemes as at this resolution, stable time step is governed by the CFL condition, not the source terms. In the case of $r_i = -r_e = 10^5/\sqrt{4\pi}$, we observe that IMEX schemes consistently outperform explicit scheme even on 800 cells as the stiffness in the source is very strong and hence it decides the stable time step for explicit schemes.

Given the similar accuracy of the explicit and IMEX schemes of the same order, and the ability of IMEX schemes to overcome time-step restriction due to stiff source terms, especially at the lower resolutions, in the remaining test cases, we will present numerical results only for the ARK-IMEX

schemes. We have also computed the results using explicit schemes (whenever source terms are not stiff) also, and the solutions are similar to those of the IMEX schemes of the same order.

6.1.3 Self-similar current sheet with finite resistivity

In this test case, we consider a self-similar current sheet which includes the finite resistivity effects. The test case was first considered in [10], and the two-fluid relativistic extension is presented in [12], which is used here. We consider the modified Equations (40a) and (40b) to capture the resistive effects.

For resistive RMHD solution [10], only the B_y -component has non-zero variation, whose time evolution includes the resistive effects and is governed by the diffusion equation,

$$\frac{\partial B_y}{\partial t} - D \frac{\partial^2 B_y}{\partial x^2} = 0. \quad (43)$$

The relation between the diffusion coefficient and resistivity constant is given by the expression $D = \eta c^2$. An exact self similar solution of Eqn. (43) in the resistive RMHD regime [10] is given by

$$B_y(x, t) = B_0 \operatorname{erf}\left(\frac{x}{2\sqrt{Dt}}\right),$$

where “erf” is the error function.

For two-fluid relativistic plasma equations, we consider the initial B_y at the time $t = 1.0$, using $B_0 = 1.0$ and $\eta c^2 = 0.01$. The domain is $[-1.5, 1.5]$ with Neumann boundary conditions. The charge to mass ratios are $r_i = -r_e = 10^3$. The ion and electron density are 0.5, and the ion and electron pressure are 25.0. The z -component of the ion and electron velocity is given by

$$u_{z_i} = -u_{z_e} = \frac{B_0}{r_i \rho_i \sqrt{\pi D}} \exp\left(-\frac{x^2}{4D}\right).$$

All other variables are set to zero. We evolve the solution from the initial time $t = 1$ to final time $t = 9.0$ using ARK-IMEX schemes **O2-ES-IMEX**, **O3-ES-IMEX** and **O4-ES-IMEX**. The solutions using 400 cells are plotted in Figure (3). We observe that, in the presence of friction terms as in Eqn. (40a), (40b), the obtained B_y profile for all the schemes matches with the resistive RMHD analytical expression of the B_y -component. Furthermore, all the schemes are highly accurate and there is no visible difference in the solution profiles.

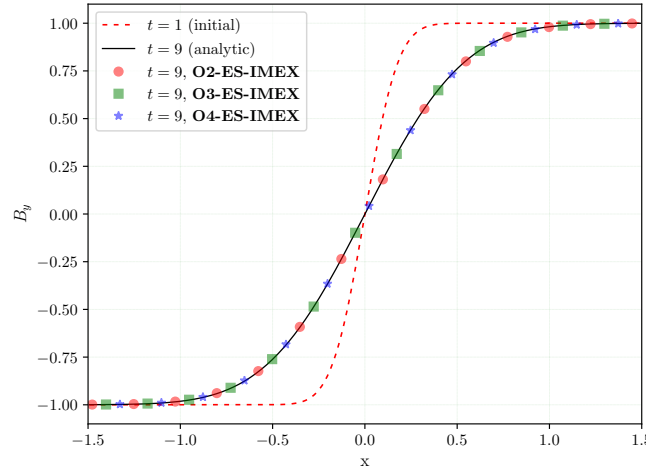


Figure 3: **Self-similar current sheet with finite resistivity**: Comparison of the B_y profile for ARK-IMEX schemes (**O2-ES-IMEX**, **O3-ES-IMEX**, and **O4-ES-IMEX**) using 400 cells.

6.2 Two-dimensional test cases

For two-dimensional test cases, the time step is chosen using,

$$\Delta t = \text{CFL} \cdot \min \left\{ \left(\frac{\Delta x}{\Lambda_{\max}^x(\mathbf{U}_{i,j})} + \frac{\Delta y}{\Lambda_{\max}^y(\mathbf{U}_{i,j})} \right) : 1 \leq i \leq N_x, 1 \leq y \leq N_y \right\}$$

where $\Lambda_{\max}^x(\mathbf{U}_{i,j}) = \max\{|\Lambda_k^x(\mathbf{U}_{i,j})| : 1 \leq k \leq 16\}$ and $\Lambda_{\max}^y(\mathbf{U}_{i,j}) = \max\{|\Lambda_k^y(\mathbf{U}_{i,j})| : 1 \leq k \leq 16\}$. We take CFL to be 0.45 and present the numerical results for the ARK-IMEX schemes (**O3-ES-IMEX**, and **O4-ES-IMEX**). We have not presented the results for second-order scheme **O2-ES-IMEX** as the scheme is less accurate when compared to the third and fourth order schemes.

6.2.1 Relativistic Orzag-Tang test case

Orzag-Tang test case was first proposed for the non-relativistic MHD systems in [48]. Here, we consider the two-fluid relativistic extension of the test case, presented in [29]. To have consistent comparison with the results in [29], we consider the Maxwell's equations with scaled source (42). We consider the computational domain $[0.0, 1.0] \times [0.0, 1.0]$ with periodic boundary conditions. The initial conditions are given by,

$$\begin{pmatrix} \rho_i \\ u_{x_i} \\ u_{y_i} \\ p_i \end{pmatrix} = \begin{pmatrix} \frac{25}{72\pi} \\ -\frac{\sin(2\pi y)}{2} \\ \frac{\sin(2\pi x)}{2} \\ \frac{2}{24\pi} \end{pmatrix}, \quad \begin{pmatrix} \rho_e \\ u_{x_e} \\ u_{y_e} \\ p_e \end{pmatrix} = \begin{pmatrix} \frac{25}{72\pi} \\ -\frac{\sin(2\pi y)}{2} \\ \frac{\sin(2\pi x)}{2} \\ \frac{2}{24\pi} \end{pmatrix}, \quad \begin{pmatrix} B_x \\ B_y \end{pmatrix} = \begin{pmatrix} -\sin(2\pi y) \\ \sin(4\pi x) \end{pmatrix}$$

The initial electric field is given by $-\mathbf{u}_i \times \mathbf{B}$ and all other variables are set to zero. We use the charge to mass ratios of $r_i = -r_e = 10^3/\sqrt{4\pi}$, thus the plasma skin depth approximates to 3.0×10^{-3} . We choose adiabatic indices $\gamma_i = \gamma_e = 5/3$ and simulate till time $t = 1.0$ on a mesh with 200×200 cells.

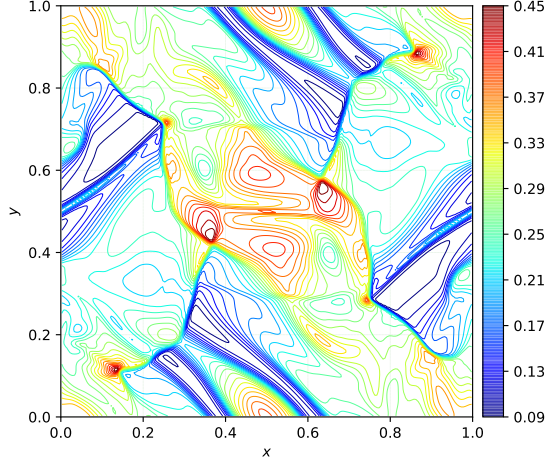
In Figure (4) and (5), we have plotted the total density, total pressure, ion Lorentz factor and magnitude of the magnetic field for **O3-ES-IMEX** and **O4-ES-IMEX** schemes, respectively. The results for both the schemes are comparable to those in [29]. Furthermore, both the schemes have similar performance. As the cell size is higher than the plasma skin depth, the solution is comparable to those of the RMHD case.

In Figure (6), we plot the time evolution of the total fluid entropy $\mathcal{U}_i + \mathcal{U}_e$ for **O3-ES-IMEX** and **O4-ES-IMEX** schemes. Initially, we do not see significant decay as discontinuities are not present in the solution. However, at time approximately $t = 0.4$, the solutions start to develop discontinuities and we see sharp decay in the entropies. We also observe that third-order scheme decays slightly more entropy than the fourth-order scheme, however, the difference is very small.

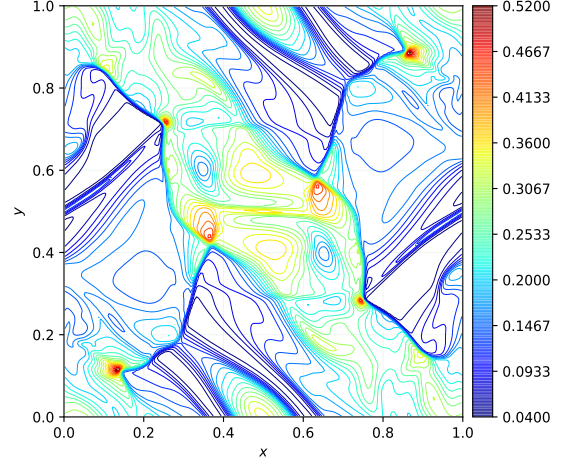
6.2.2 Relativistic two-fluid blast problem

We consider the two-fluid relativistic extension of the strong cylindrical RMHD explosion described in [6]. We follow [12, 29] to consider a computational domain of $[-6, 6] \times [-6, 6]$ with Neumann boundary conditions. To describe the initial fluid profile, consider $\rho_{in} = 10^{-2}$, $p_{in} = 1.0$, $\rho_{out} = 10^{-4}$ and $p_{out} = 5 \times 10^{-4}$. Also, let us denote the radial distance $r = \sqrt{x^2 + y^2}$ from the center of the computational domain. Inside the disc of radius 0.8, i.e., $r < 0.8$, we define the densities $\rho_i = \rho_e = 0.5 \times \rho_{in}$ and the pressures $p_i = p_e = 0.5 \times p_{in}$. Also, outside the disc of radius 1.0, i.e., $r > 1.0$, we define the densities $\rho_i = \rho_e = 0.5 \times \rho_{out}$ and the pressures $p_i = p_e = 0.5 \times p_{out}$. In the range $0.8 \leq r \leq 1.0$, the densities and pressures are defined using a linear profile, such that the densities and the pressures decreases with increase in the radius r and at the boundaries $r = 0.8$ and $r = 1.0$ they matches the prescribed constant states. The magnetic field has been initialized in the x -direction only, as $B_x = B_0$. We set all remaining variables to zero. The charge to mass ratios are taken to be $r_i = -r_e = 10^3$ and $\gamma_i = \gamma_e = 4/3$.

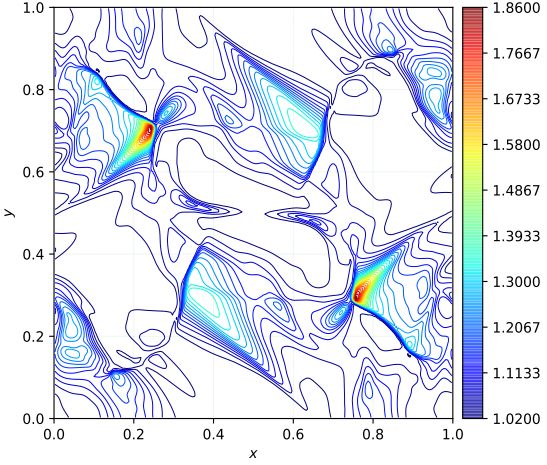
We compute solutions on a mesh of 200×200 cells using the **O3-ES-IMEX** and **O4-ES-IMEX** schemes till final time $t = 4.0$. We consider two values of parameter B_0 , such that $B_0 = 0.1$ denoting the case of the weakly magnetized medium, and $B_0 = 1.0$ denoting the case of the strongly magnetized medium. In Figures (7) and (8), we plot the results for weakly magnetized medium for **O3-ES-IMEX** and **O4-ES-IMEX** schemes, respectively. We have plotted the log to the base 10 of total density and



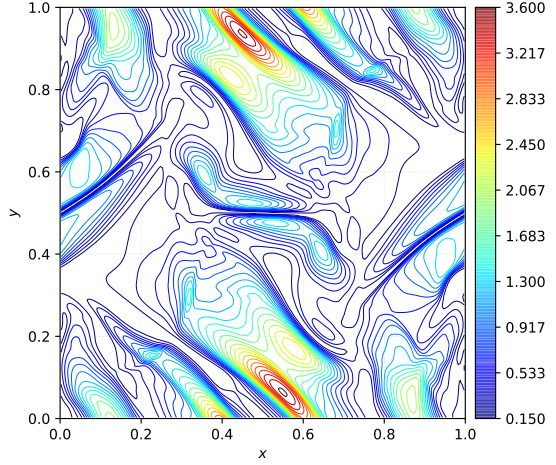
(a) Plot of total density $\rho_i + \rho_e$.



(b) Plot of total pressure $p_i + p_e$.

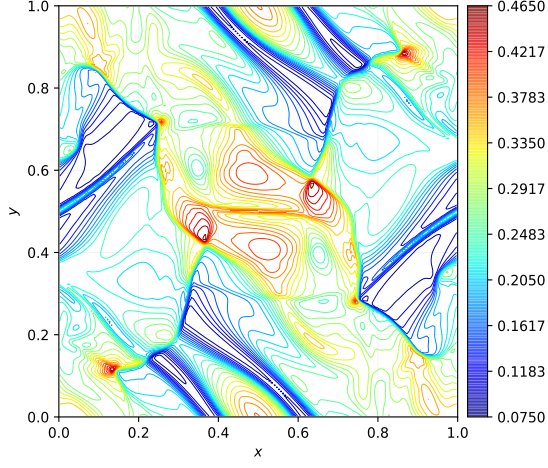


(c) Plot of ion Lorentz factor Γ_i .

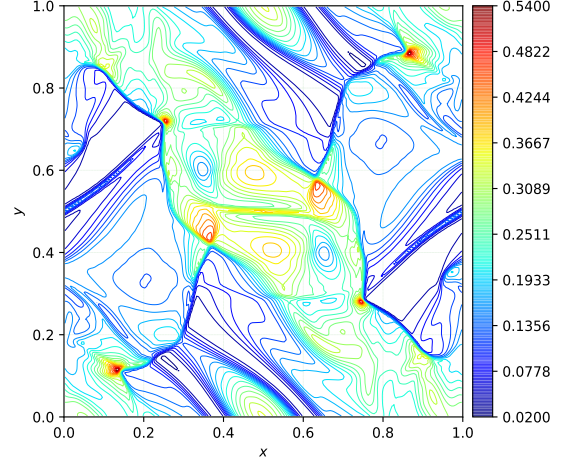


(d) Plot of magnitude of the Magnetic field, $\frac{|\mathbf{B}|^2}{2}$.

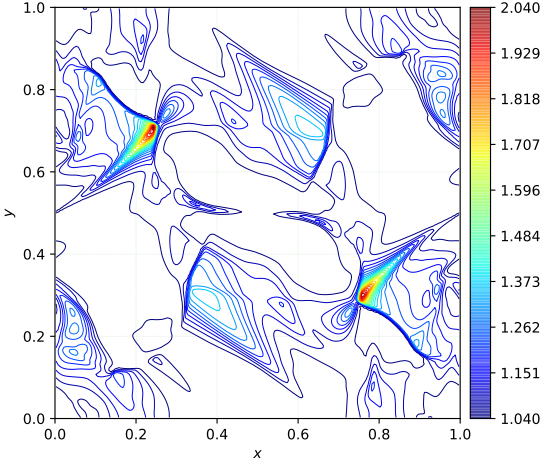
Figure 4: **Relativistic Orzag-Tang test case**: Plots of total density, total pressure, Ion Lorentz factor, and magnitude of magnetic field $\frac{|\mathbf{B}|^2}{2}$ using **O3-ES-IMEX** scheme and 200×200 cells at time $t = 0.1$. We have plotted 30 contours for each variable.



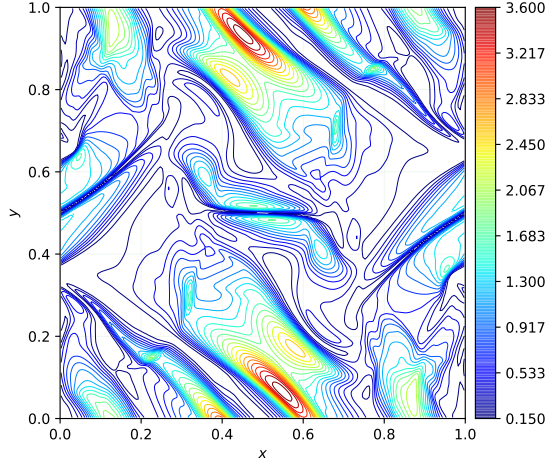
(a) Plot of total density $\rho_i + \rho_e$.



(b) Plot of total pressure $p_i + p_e$.



(c) Plot of ion Lorentz factor Γ_i .



(d) Plot of magnitude of the Magnetic field, $\frac{|\mathbf{B}|^2}{2}$.

Figure 5: **Relativistic Orzag-Tang test case**: Plots of total density, total pressure, Ion Lorentz factor, and magnitude of magnetic field $\frac{|\mathbf{B}|^2}{2}$ using **O4-ES-IMEX** scheme and 200×200 cells at time $t = 0.1$. We have plotted 30 contours for each variable.

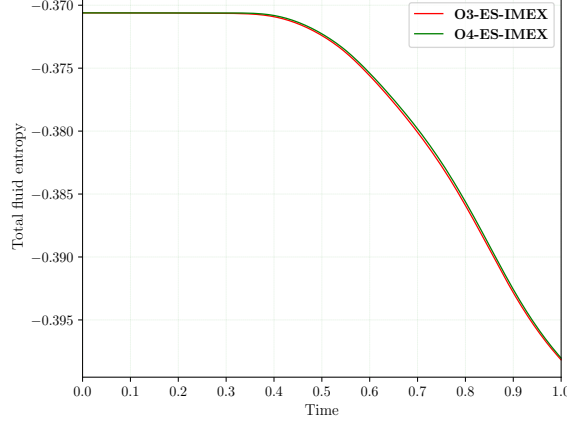


Figure 6: **Relativistic Orzag-Tang test case**: Total fluid entropy $\mathcal{U}_i + \mathcal{U}_e$ evolution for the schemes **ES-O3-IMEX** and **ES-O4-IMEX**.

total pressure; we also plot the ion Lorentz factor and magnitude of the magnetic field. We observe that both the schemes produce stable results and are able to capture the waves accurately. Furthermore, the results are comparable to those in [12] and [29].

Similarly, in the case of strongly magnetized medium we plot the results for **O3-ES-IMEX** and **O4-ES-IMEX** schemes in Figures (9) and (10), respectively. We observe a substantial change in the solution profile. Again both the schemes are able to capture the blast waves accurately.

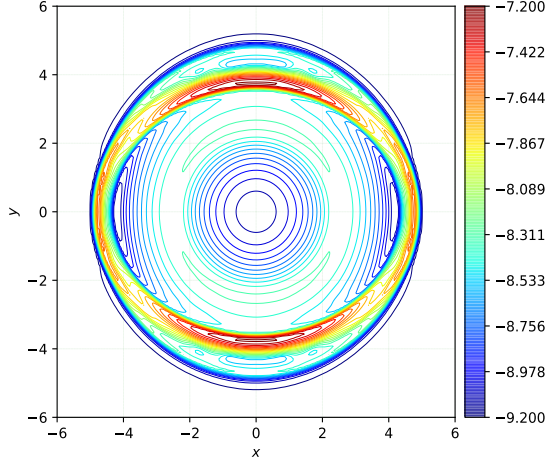
In Figure (11), we plot the evolution of the total fluid entropy $\mathcal{U}_i + \mathcal{U}_e$ for the **O3-ES-IMEX** and **O4-ES-IMEX** schemes in weakly and strongly magnetized mediums. As the solutions contain many discontinuities, we see a strong decay in the entropies. Furthermore, **O4-ES-IMEX** scheme decays less entropy than the **O3-ES-IMEX** scheme.

6.2.3 Relativistic two-fluid GEM challenge problem

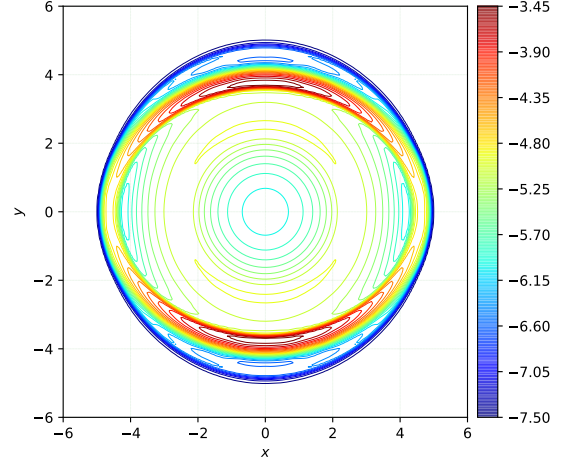
In this test, we consider two-fluid relativistic Geospace Environment Modeling (GEM) magnetic reconnection problem from [12], which is an extension of the non-relativistic GEM magnetic reconnection given in [49]. We consider the modified Equations (40a) and (40b) to capture the resistive effects. The computational domain is $[-L_x/2, L_x/2] \times [-L_y/2, L_y/2]$ where $L_x = 8\pi$ and $L_y = 4\pi$, with periodic boundary conditions at $x = \pm L_x/2$ and conducting wall boundary at $y = \pm L_y/2$ boundary. The ion-electron mass ratio is taken to be $m_i/m_e = 25$ with $m_i = 1$. Accordingly, we have $r_i = 1.0$ and $r_e = -25.0$. The unperturbed x -component of the magnetic field is taken to be $B_x(y) = B_0 \tan(y/d)$ with $B_0 = 1.0$, where $d = 1.0$ is the thickness of the current sheet. On the other hand, unperturbed y - and z -components of the magnetic field are assumed to be zero. After the perturbation initial conditions become

$$\begin{pmatrix} \rho_i \\ u_{z_i} \\ p_i \\ \rho_e \\ u_{z_e} \\ p_e \\ B_x \\ B_y \end{pmatrix} = \begin{pmatrix} n \\ \frac{c}{2d} \frac{B_0 \text{sech}^2(y/d)}{n^2} \\ 0.2 + \frac{B_0^2 \text{sech}^2(y/d)}{4} \frac{5}{24\pi} \\ \frac{m_e}{m_p} n \\ -(u_z)_i \\ -p_i \\ B_0 \tan(y/d) - B_0 \psi_0 \frac{\pi}{L_y} \cos\left(\frac{\pi x}{L_x}\right) \sin\left(\frac{\pi y}{L_y}\right) \\ B_0 \psi_0 \frac{\pi}{L_x} \sin\left(\frac{\pi x}{L_x}\right) \cos\left(\frac{\pi y}{L_y}\right) \end{pmatrix}$$

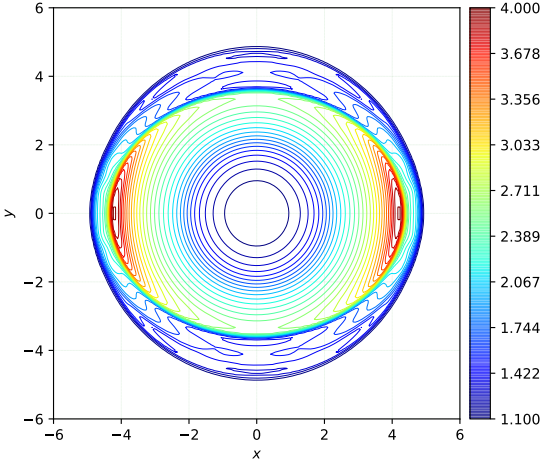
where $n = \text{sech}^2(y/d) + 0.2$. All other variables are set to zero. We set resistivity constant as $\eta = 0.01$, and adiabatic indices as $\gamma_i = \gamma_e = 4.0/3.0$.



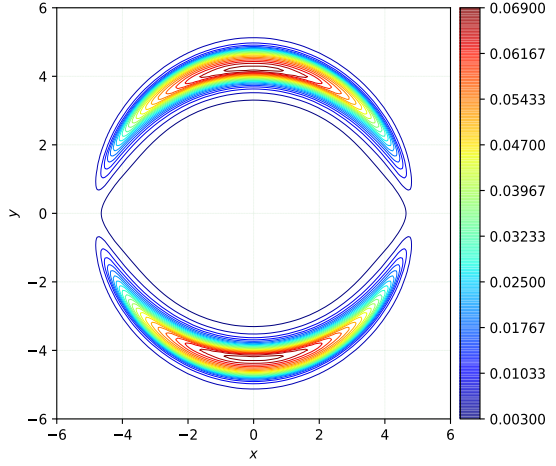
(a) Plot of $\log_{10}(\rho_i + \rho_e)$.



(b) Plot of $\log_{10}(p_i + p_e)$.

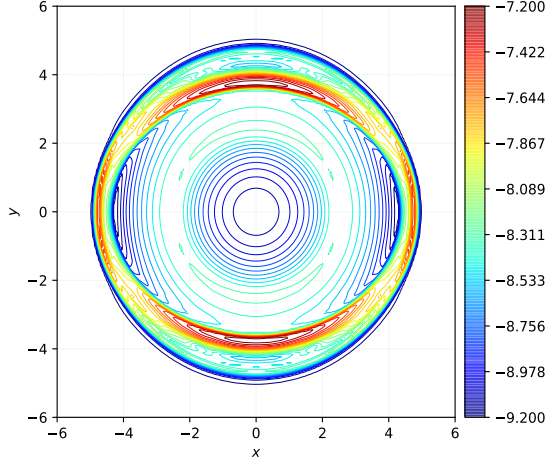


(c) Ion Lorentz factor Γ_i .

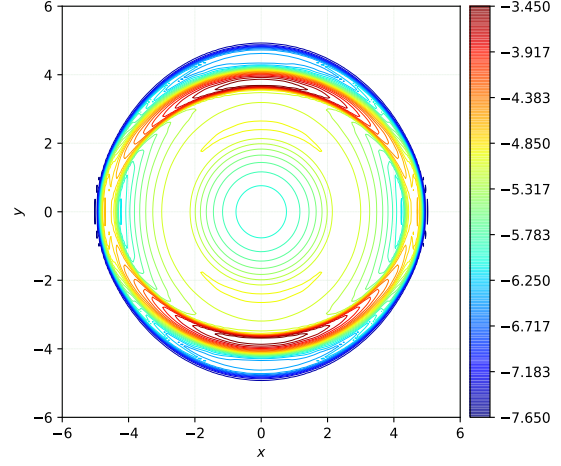


(d) Magnitude of the Magnetic field $\frac{|\mathbf{B}|^2}{2}$.

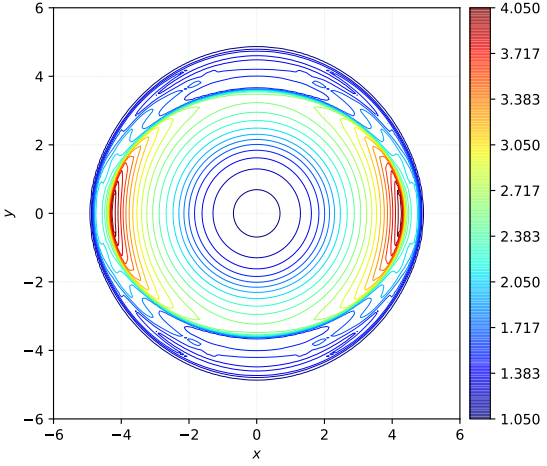
Figure 7: **Relativistic two-fluid blast problem**: Plot for the weakly magnetized medium $B_0 = 0.1$, using **O3-ES-IMEX** scheme with 200×200 cells. We have plotted 30 contours for each variable.



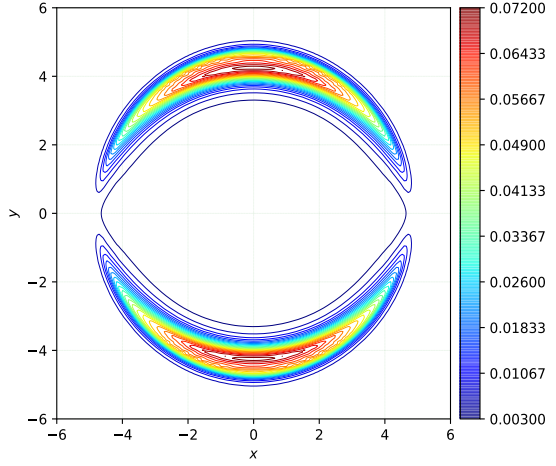
(a) Plot of $\log_{10}(\rho_i + \rho_e)$.



(b) Plot of $\log_{10}(p_i + p_e)$.

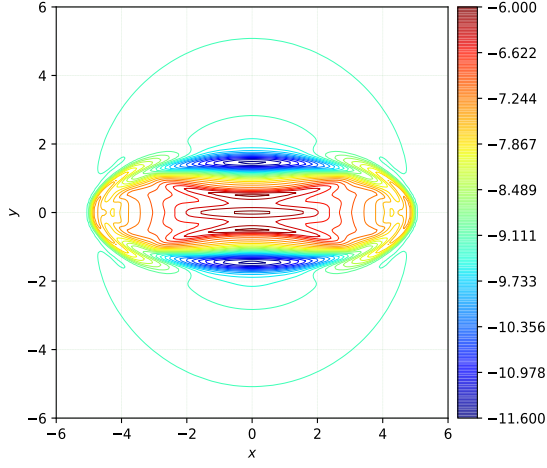


(c) Plot of ion Lorentz factor Γ_i .

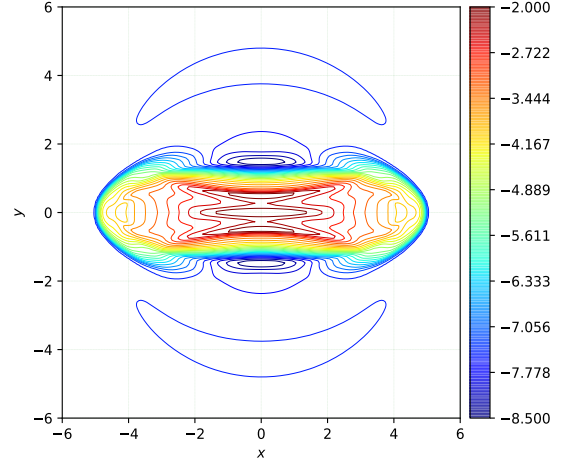


(d) Plot of magnitude of the Magnetic field $\frac{|\mathbf{B}|^2}{2}$.

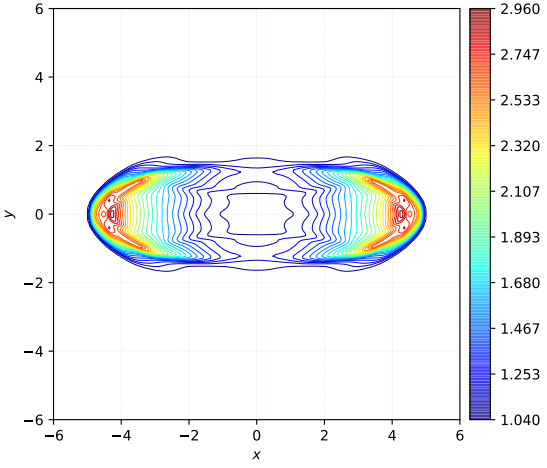
Figure 8: **Relativistic two-fluid blast problem**: Plot for the weakly magnetized medium $B_0 = 0.1$, using **O4-ES-IMEX** scheme with 200×200 cells. We have plotted 30 contours for each variable.



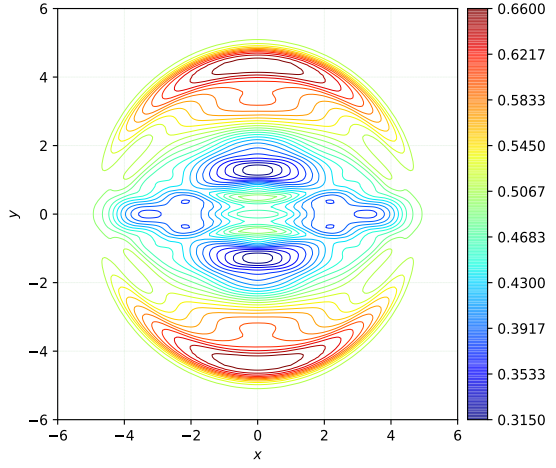
(a) Plot of $\log_{10}(\rho_i + \rho_e)$.



(b) Plot of $\log_{10}(p_i + p_e)$.

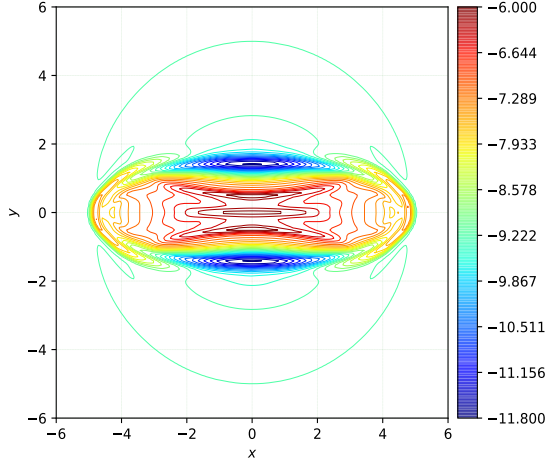


(c) Plot of ion Lorentz factor Γ_i .

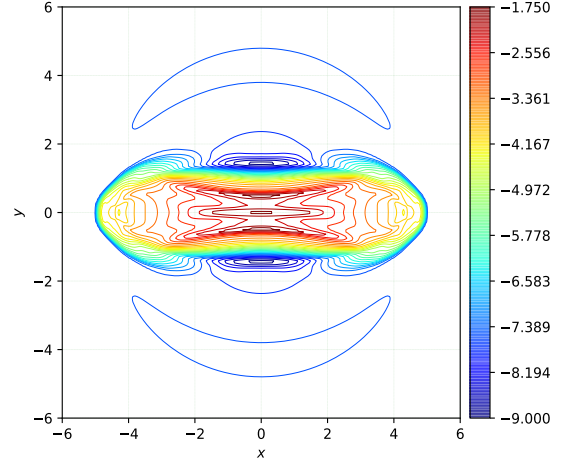


(d) Plot of magnitude of the Magnetic field $\frac{|\mathbf{B}|^2}{2}$.

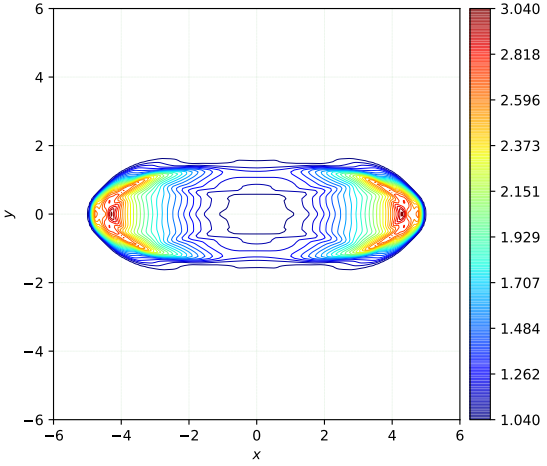
Figure 9: **Relativistic two-fluid blast problem**: Plot for the strongly magnetized medium $B_0 = 1.0$, using **O3-ES-IMEX** scheme with 200×200 cells. We have plotted 30 contours for each variable.



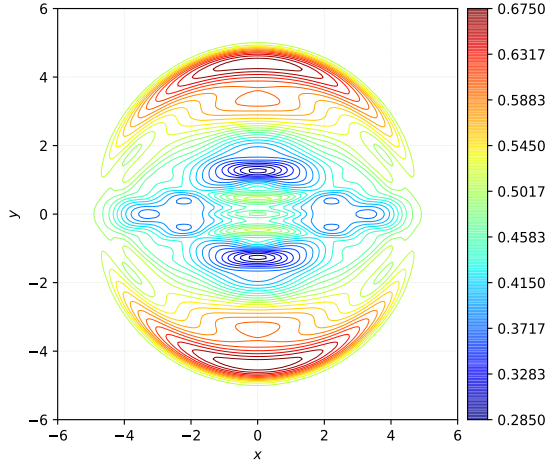
(a) Plot of $\log_{10}(\rho_i + \rho_e)$.



(b) Plot of $\log_{10}(p_i + p_e)$.

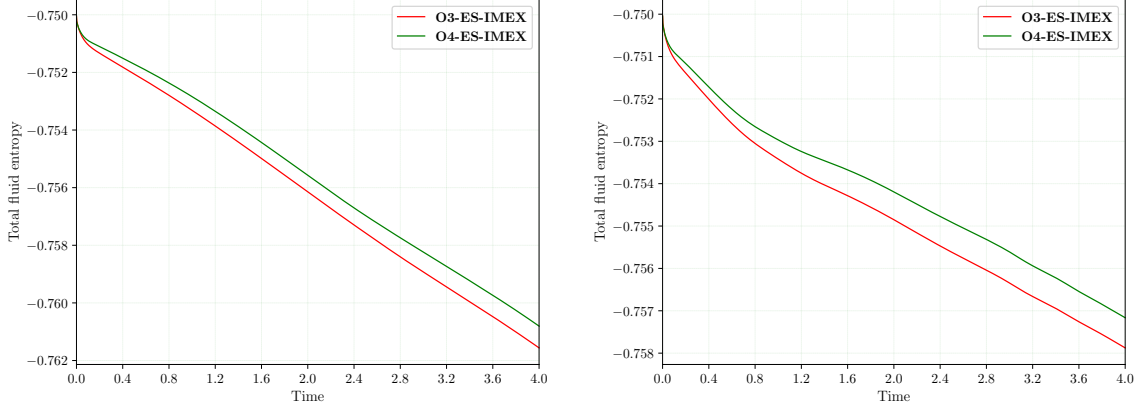


(c) Plot of ion Lorentz factor Γ_i .



(d) Plot magnitude of the Magnetic field $\frac{|\mathbf{B}|^2}{2}$.

Figure 10: **Relativistic two-fluid blast problem**: Plot for the strongly magnetized medium $B_0 = 1.0$, using **O4-ES-IMEX** scheme with 200×200 cells. We have plotted 30 contours for each variable.



(a) Total entropy fluid decay for weakly magnetized medium, $B_0 = 0.1$. (b) Total fluid entropy decay for strongly magnetized medium, $B_0 = 1.0$.

Figure 11: **Relativistic two-fluid blast problem**: Total fluid entropy $\mathcal{U}_i + \mathcal{U}_e$ evolution of the schemes **ES-O3-IMEX** and **ES-O4-IMEX** for the weakly and strongly magnetized medium.

We plot total density, z -component of magnetic field, x -component of ion velocity and x -component of electron velocity on a mesh of 512×256 cells. The plots also contain field line for (B_x, B_y) . We plot the solution at $t = 40$ and $t = 80$ for **O3-ES-IMEX** and **O4-ES-IMEX**. We observe that both the solutions for both the schemes are similar and agrees with the solutions presented in [12].

In Figure (16), we also plot time evolution of the reconnected magnetic flux,

$$\psi(t) = \frac{1}{2B_0} \int_{-L_x/2}^{L_x/2} |B_y(x, y=0, t)| dx.$$

at various resolutions. We also compare it with the results presented in [12]. We observe that both schemes are able to capture the reconnected flux at various resolutions. Only for the time more than $t = 80$, we see a difference in the reconnection flux for the different schemes, but at this time, flow is already quite turbulent.

7 Conclusion

The two-fluid relativistic plasma flow equations are a multi-physics model that couples relativistic hydrodynamic conservation laws with Maxwell's equations. This model is non-linear and exhibits non-smooth and multi-scale phenomena. In this article, we have designed arbitrary high-order finite-difference entropy stable schemes for the model. This was achieved by exploiting the structure of the flux and by demonstrating that the source terms do not contribute to the fluid entropies. Furthermore, we have also presented ARK-IMEX schemes to overcome the time-step restriction imposed by the stiff source terms. The implicit step in the ARK-IMEX scheme is efficient as it involves solving only one set of nonlinear equations in each cell and there is no need for any global nonlinear solver.

The proposed schemes are then tested on various test cases in one and two dimensions. First, we demonstrate that the proposed schemes have formal order of accuracy. Then we test the schemes on the Brio-Wu test problem, where we have finite plasma skin depth. We note that the proposed schemes can resolve the dispersive effects, and higher-order schemes can capture the finite skin depth effects even on coarser meshes. We also demonstrate that on the coarser meshes with the stiff source terms, IMEX schemes are highly efficient. The SSP-RK and ARK-IMEX schemes have similar accuracy and entropy decay performance. We then test the scheme on a current sheet problem where resistive effects are considered. We observe that the proposed schemes accurately capture the RMHD solution. We compute the Orzag-Tang vortex, blast problem, and GEM challenge problem in two-dimensional test cases. We

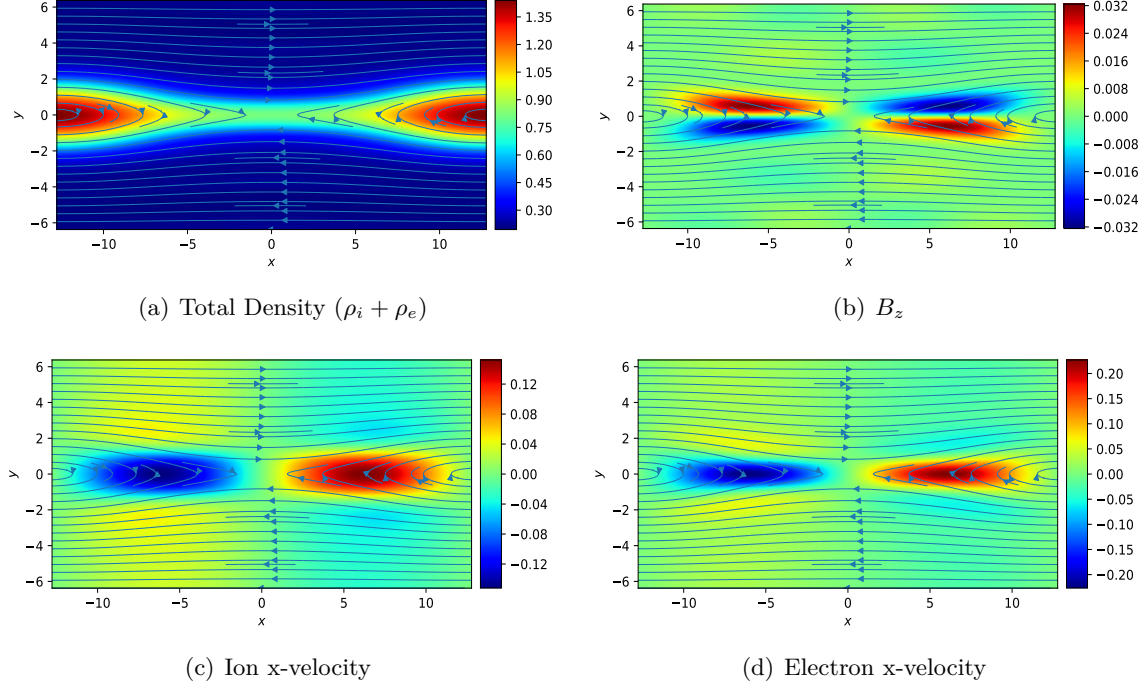


Figure 12: [Relativistic two-fluid GEM challenge problem](#): Plots for the total density, B_z -component, Ion x -velocity, and Electron x -velocity on the mesh 512×256 , using scheme **O3-ES-IMEX**, at time $t=40.0$.

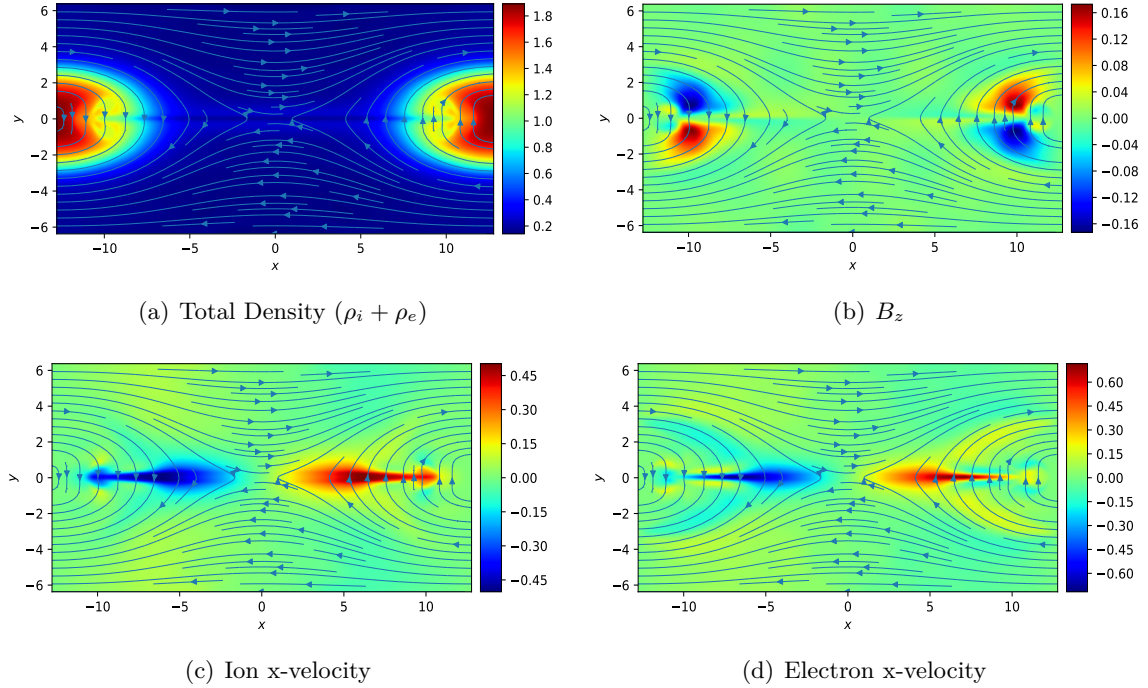


Figure 13: [Relativistic two-fluid GEM challenge problem](#): Plots for the total density, B_z -component, Ion x -velocity, and Electron x -velocity on the mesh 512×256 , using scheme **O3-ES-IMEX**, at time $t=80.0$.

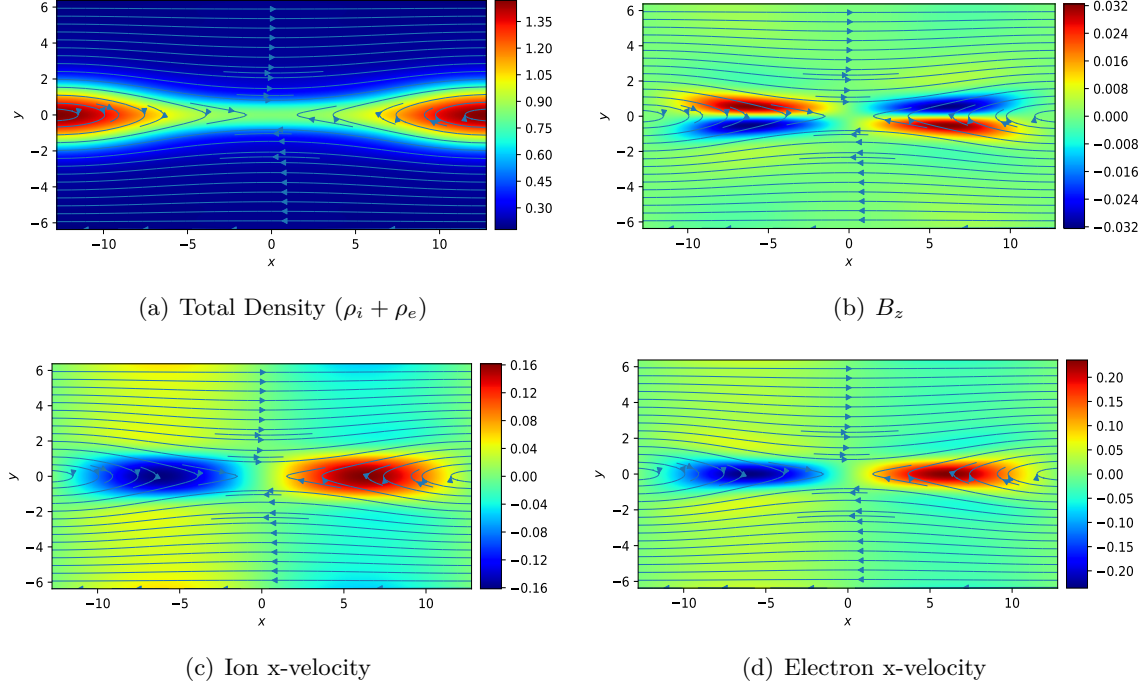


Figure 14: Relativistic two-fluid GEM challenge problem: Plot for the total density, B_z -component, Ion x -velocity, and Electron x -velocity on the mesh 512×256 , using scheme **O4-ES-IMEX**, at time $t=40.0$.

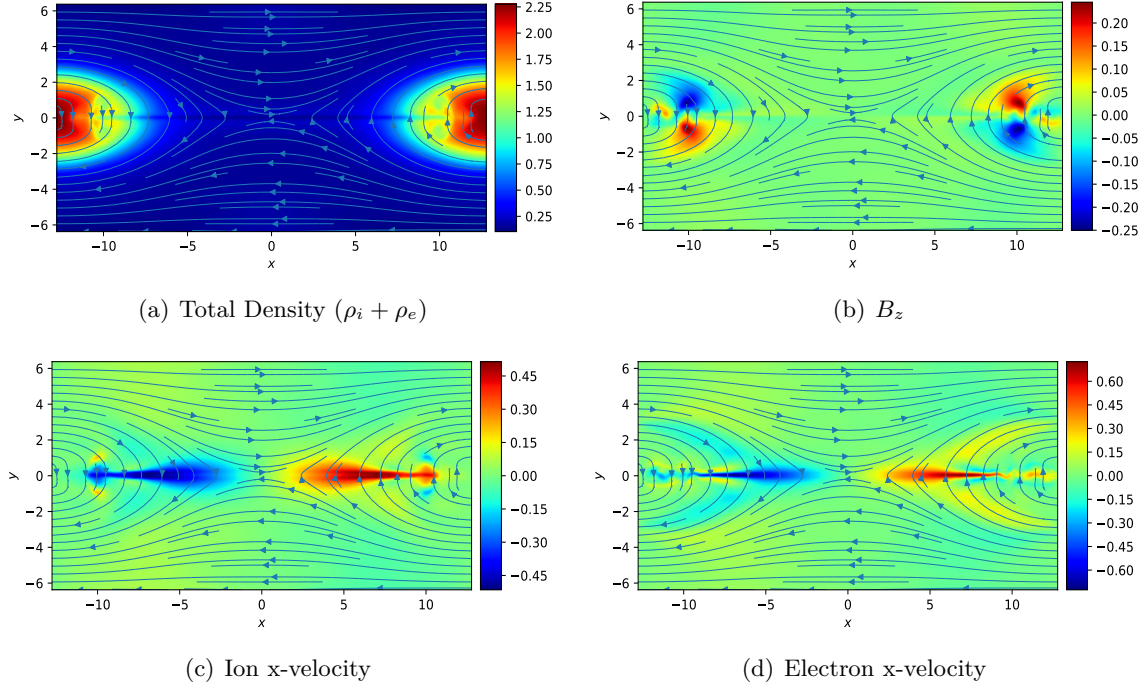


Figure 15: Relativistic two-fluid GEM challenge problem: Plot for the total Density, B_z -component, Ion x -velocity, and Electron x -velocity on the mesh 512×256 , using scheme **O4-ES-IMEX**, at time $t=80.0$.

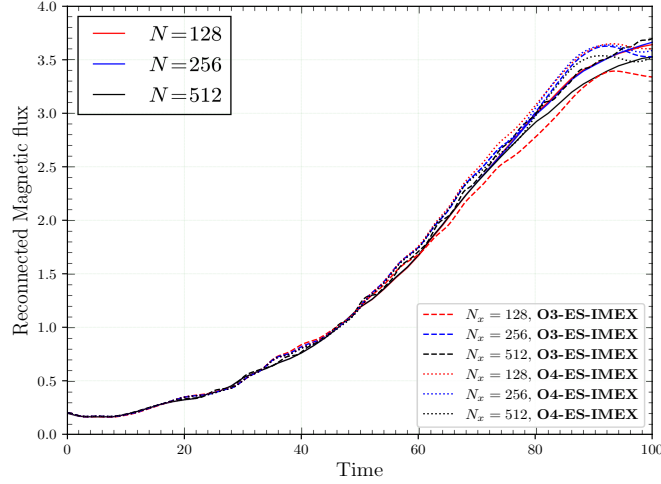


Figure 16: **Relativistic two-fluid GEM challenge problem**: Time development of the reconnected magnetic flux for $N_x = 128, 256, 512$, using schemes **O3-ES-IMEX** and **O4-ES-IMEX**. We overlay the plot on Amano's GEM data [12] (solid lines).

again show that the schemes are able to capture solution features very well and ensure entropy stability of the solutions. For the GEM problem, the schemes are also able to predict magnetic reconnection flux.

Acknowledgments

The work of Harish Kumar is supported by VAJRA grant No. VJR/2018/000129 by the Dept. of Science and Technology, Govt. of India. The work of Praveen Chandrashekar was supported by SERB-DST, Govt. of India, under the MATRICS grant No. MTR/2018/000006, and by the Department of Atomic Energy, Government of India, under project no. 12-R&D-TFR-5.01-0520. The authors would also like to thank Prof. Dinshaw Balsara, Univ. of Notre-Dame, USA, for his several suggestions.

References

- [1] D. Bhojia, H. Kumar, Entropy-stable schemes for relativistic hydrodynamics equations, Zeitschrift für Angewandte Mathematik und Physik 71 (1) (2020). doi:10.1007/s00033-020-1250-8.
- [2] Y. A. Gallant, J. Arons, Structure of relativistic shocks in pulsar winds: A model of the wisps in the Crab Nebula, The Astrophysical Journal 435 (1994) 230. doi:10.1086/174810.
- [3] R. Mochkovitch, V. Maitia, R. Marques, Internal shocks in a relativistic wind as a source for gamma-ray bursts?, Astrophysics and Space Science 231 (1-2) (1995) 441–444. doi:10.1007/BF00658666.
- [4] L. D. Landau, E. M. Lifshitz, Relativistic Fluid Dynamics, in: Fluid Mechanics, Elsevier, 1987, pp. 505–514. doi:10.1016/b978-0-08-033933-7.50023-4.
- [5] J. F. Wardle, D. C. Homan, R. Ojha, D. H. Roberts, Electron-positron jets associated with the quasar 3C279, Nature 395 (6701) (1998) 457–461. doi:10.1038/26675.
- [6] S. S. Komissarov, A Godunov-type scheme for relativistic magnetohydrodynamics, Monthly Notices of the Royal Astronomical Society 303 (2) (1999) 343–366. doi:10.1046/j.1365-8711.1999.02244.x.
- [7] D. Balsara, Total Variation Diminishing Scheme for Relativistic Magnetohydrodynamics, The Astrophysical Journal Supplement Series 132 (1) (2001) 83–101. doi:10.1086/318941.

- [8] L. Del Zanna, N. Bucciantini, P. Londrillo, An efficient shock-capturing central-type scheme for multidimensional relativistic flows II. Magnetohydrodynamics, *Astronomy and Astrophysics* 400 (2) (2003) 397–413. doi:10.1051/0004-6361:20021641.
- [9] A. Mignone, G. Bodo, An HLLC Riemann solver for relativistic flows – II. Magnetohydrodynamics, *Monthly Notices of the Royal Astronomical Society* 368 (3) (2006) 1040–1054. doi:10.1111/J.1365-2966.2006.10162.X.
- [10] S. S. Komissarov, Multidimensional numerical scheme for resistive relativistic magnetohydrodynamics, *Monthly Notices of the Royal Astronomical Society* 382 (3) (2007) 995–1004. doi:10.1111/j.1365-2966.2007.12448.x.
- [11] D. S. Balsara, J. Kim, A subluminal relativistic magnetohydrodynamics scheme with ADER-WENO predictor and multidimensional Riemann solver-based corrector, *Journal of Computational Physics* 312 (2016) 357–384. doi:10.1016/j.jcp.2016.02.001.
- [12] T. Amano, A second-order divergence-constrained multidimensional numerical scheme for Relativistic Two-Fluid Electrodynamics, *The Astrophysical Journal* 831 (1) (2016) 100. doi:10.3847/0004-637x/831/1/100.
- [13] U. Shumlak, J. Loverich, Approximate Riemann solver for the two-fluid plasma model, *Journal of Computational Physics* 187 (2) (2003) 620–638. doi:10.1016/S0021-9991(03)00151-7.
- [14] A. Hakim, J. Loverich, U. Shumlak, A high resolution wave propagation scheme for ideal Two-Fluid plasma equations, *Journal of Computational Physics* 219 (1) (2006) 418–442. doi:10.1016/j.jcp.2006.03.036.
- [15] H. Kumar, S. Mishra, Entropy stable numerical schemes for two-fluid plasma equations, *Journal of Scientific Computing* 52 (2) (2012) 401–425. doi:10.1007/s10915-011-9554-7.
- [16] R. Abgrall, H. Kumar, Robust Finite Volume Schemes for Two-Fluid Plasma Equations, *Journal of Scientific Computing* 60 (3) (2014) 584–611. doi:10.1007/s10915-013-9809-6.
- [17] D. M. Bond, V. Wheatley, R. Samtaney, Plasma flow simulation using the two-fluid model, in: *Proceedings of the 20th Australasian Fluid Mechanics Conference*, 2016.
- [18] Y. Li, R. Samtaney, D. Bond, V. Wheatley, Richtmyer-Meshkov instability of an imploding flow with a two-fluid plasma model, *Physical Review Fluids* 5 (11) (2020) 113701. doi:10.1103/PhysRevFluids.5.113701.
- [19] A. K. Meena, H. Kumar, Robust numerical schemes for Two-Fluid Ten-Moment plasma flow equations, *Zeitschrift für Angewandte Mathematik und Physik* 70 (1) (2019) 1–30. doi:10.1007/s00033-018-1061-3.
- [20] S. Zenitani, M. Hesse, A. Klimas, Relativistic two-fluid simulations of guide field magnetic reconnection, *Astrophysical Journal* 705 (1) (2009) 907–913. doi:10.1088/0004-637X/705/1/907.
- [21] S. Zenitani, M. Hesse, A. Klimas, Resistive magnetohydrodynamic simulations of relativistic magnetic reconnection, *Astrophysical Journal Letters* 716 (2) (2010) L214–L218. doi:10.1088/2041-8205/716/2/L214.
- [22] T. Amano, J. G. Kirk, The role of superluminal electromagnetic waves in pulsar wind termination shocks, *Astrophysical Journal* 770 (1) (2013) 18. doi:10.1088/0004-637X/770/1/18.
- [23] M. Barkov, S. S. Komissarov, V. Korolev, A. Zankovich, A multidimensional numerical scheme for two-fluid relativistic magnetohydrodynamics, *Monthly Notices of the Royal Astronomical Society* 438 (1) (2014) 704–716. doi:10.1093/mnras/stt2247.
- [24] M. V. Barkov, S. S. Komissarov, Relativistic tearing and drift-kink instabilities in two-fluid simulations, *Monthly Notices of the Royal Astronomical Society* 458 (2) (2016) 1939–1947. doi:10.1093/mnras/stw384.
- [25] R. J. LeVeque, *Finite Volume Methods for Hyperbolic Problems*, Cambridge University Press, 2002. doi:10.1017/cbo9780511791253.

- [26] E. Chiodaroli, C. De Lellis, O. Kreml, Global Ill-Posedness of the Isentropic System of Gas Dynamics, *Communications on Pure and Applied Mathematics* 68 (7) (2015) 1157–1190. doi:
10.1002/CPA.21537.
- [27] E. Godlewski, P.-A. Raviart, Numerical Approximation of Hyperbolic Systems of Conservation Laws, Vol. 118 of Applied Mathematical Sciences, Springer New York, New York, NY, 1996. doi:
10.1007/978-1-4612-0713-9.
- [28] S. Zenitani, M. Hesse, A. Klimas, Two-fluid magnetohydrodynamic simulations of relativistic magnetic reconnection, *Astrophysical Journal* 696 (2) (2009) 1385–1401. doi:10.1088/0004-637X/696/
2/1385.
- [29] D. S. Balsara, T. Amano, S. Garain, J. Kim, A high-order relativistic two-fluid electrodynamic scheme with consistent reconstruction of electromagnetic fields and a multidimensional Riemann solver for electromagnetism, *Journal of Computational Physics* 318 (2016) 169–200. doi:10.1016/
j.jcp.2016.05.006.
- [30] U. S. Fjordholm, S. Mishra, E. Tadmor, Arbitrarily high-order accurate entropy stable essentially nonoscillatory schemes for systems of conservation laws, *SIAM Journal on Numerical Analysis* 50 (2) (2012) 544–573. doi:10.1137/110836961.
- [31] U. S. Fjordholm, S. Mishra, E. Tadmor, ENO Reconstruction and ENO Interpolation Are Stable, *Foundations of Computational Mathematics* 13 (2) (2013) 139–159. doi:10.1007/
s10208-012-9117-9.
- [32] P. Chandrashekar, Kinetic energy preserving and entropy stable finite volume schemes for compressible euler and Navier-Stokes equations, *Communications in Computational Physics* 14 (5) (2013) 1252–1286. doi:10.4208/cicp.170712.010313a.
- [33] C. Sen, H. Kumar, Entropy Stable Schemes For Ten-Moment Gaussian Closure Equations, *Journal of Scientific Computing* 75 (2) (2018) 1128–1155. doi:10.1007/S10915-017-0579-4/FIGURES/8.
- [34] J. Duan, H. Tang, High-order accurate entropy stable finite difference schemes for the shallow water magnetohydrodynamics, *Journal of Computational Physics* 431 (2021) 110136. doi:10.1016/J.
JCP.2021.110136.
- [35] J. Duan, H. Tang, High-Order Accurate Entropy Stable Finite Difference Schemes for One- And Two-Dimensional Special Relativistic Hydrodynamics, *Advances in Applied Mathematics and Mechanics* 12 (1) (2020) 1–29. doi:10.4208/AAMM.OA-2019-0124.
- [36] B. Biswas, H. Kumar, D. Bhoriya, Entropy stable discontinuous Galerkin schemes for the special relativistic hydrodynamics equations, *Computers & Mathematics with Applications* 112 (September 2021) (2022) 55–75. doi:10.1016/j.camwa.2022.02.019.
- [37] C. D. Munz, P. Omnes, R. Schneider, E. Sonnendrücker, U. Voß, Divergence Correction Techniques for Maxwell Solvers Based on a Hyperbolic Model, *Journal of Computational Physics* 161 (2) (2000) 484–511. doi:10.1006/jcph.2000.6507.
- [38] V. Schneider, U. Katscher, D. H. Rischke, B. Waldhauser, J. A. Maruhn, C. D. Munz, New Algorithms for Ultra-relativistic Numerical Hydrodynamics, *Journal of Computational Physics* 105 (1) (1993) 92–107. doi:10.1006/jcph.1993.1056.
- [39] E. Tadmor, The Numerical Viscosity of Entropy Stable Schemes for Systems of Conservation Laws. I, *Mathematics of Computation* 49 (179) (1987) 91. doi:10.2307/2008251.
- [40] F. Ismail, P. L. Roe, Affordable, entropy-consistent Euler flux functions II: Entropy production at shocks, *Journal of Computational Physics* 228 (15) (2009) 5410–5436. doi:10.1016/j.jcp.2009.
04.021.
- [41] P. G. Lefloch, J. M. Mercier, C. Rohde, Fully discrete, entropy conservative schemes of arbitrary order, *SIAM Journal on Numerical Analysis* 40 (5) (2002) 1968–1992. doi:10.1137/
S003614290240069X.

- [42] T. J. Barth, Numerical methods for gas-dynamics systems on unstructured meshes, An introduction to recent developments in theory and numerics of conservation Laws, Lecture notes in computational science and engineering volume {5}, Springer, Berlin. Eds: D. Kroner, M., Springer, Berlin, Heidelberg, 1999.
- [43] G. S. Jiang, C. W. Shu, Efficient implementation of weighted ENO schemes, Journal of Computational Physics 126 (1) (1996) 202–228. [doi:10.1006/jcph.1996.0130](#).
- [44] S. Gottlieb, C. W. Shu, E. Tadmor, Strong stability-preserving high-order time discretization methods, SIAM Review 43 (1) (2001) 89–112. [doi:10.1137/S003614450036757X](#).
- [45] L. Pareschi, G. Russo, Implicit-explicit Runge-Kutta schemes and applications to hyperbolic systems with relaxation, Journal of Scientific Computing 25 (1) (2005) 129–155. [doi:10.1007/s10915-004-4636-4](#).
- [46] J. E. Dennis, R. B. Schnabel, Numerical Methods for Unconstrained Optimization and Nonlinear Equations, Society for Industrial and Applied Mathematics, 1996. [doi:10.1137/1.9781611971200](#).
- [47] C. A. Kennedy, M. H. Carpenter, Additive Runge-Kutta schemes for convection-diffusion-reaction equations, Applied Numerical Mathematics 44 (1-2) (2003) 139–181. [doi:10.1016/S0168-9274\(02\)00138-1](#).
- [48] S. A. Orszag, C. M. Tang, Small-scale structure of two-dimensional magnetohydrodynamic turbulence, Journal of Fluid Mechanics 90 (1) (1979) 129–143. [doi:10.1017/S002211207900210X](#).
- [49] J. Birn, J. F. Drake, M. A. Shay, B. N. Rogers, R. E. Denton, M. Hesse, M. Kuznetsova, Z. W. Ma, A. Bhattacharjee, A. Otto, P. L. Pritchett, Geospace Environmental Modeling (GEM) Magnetic Reconnection Challenge, Journal of Geophysical Research: Space Physics 106 (A3) (2001) 3715–3719. [doi:10.1029/1999ja900449](#).

A Barth scaling of right eigenvectors

Here, we present expressions for the right eigenvectors and scaled right eigenvectors for the conservative system (4). The right eigenvectors are described in Section A.1, while the expressions and procedure to obtain the scaled eigenvectors is presented in Section A.2

A.1 Right eigenvectors

The set of right eigenvectors of the matrix $\mathbf{A}^x = \frac{\partial \mathbf{f}^x}{\partial \mathbf{U}}$ corresponding to the eigenvalues Λ^x of the system (4) is obtained by taking $d = x$ in the ordered set $\mathbf{R}_{\Lambda^d}^d = \{(\mathbf{R}_{\Lambda^d}^d)_n : n = 1, 2, 3, \dots, 16\}$ where the vectors $(\mathbf{R}_{\Lambda^d}^d)_n$ are defined as

$$(\mathbf{R}_{\Lambda^d}^d)_n = \begin{cases} \left((\mathbf{R}_{i,k}^d)_{1 \times 5}, \mathbf{0}_{1 \times 5}, \mathbf{0}_{1 \times 6} \right)^\top, & 1 \leq n \leq 5, k = n \\ \left(\mathbf{0}_{1 \times 5}, (\mathbf{R}_{e,k}^d)_{1 \times 5}, \mathbf{0}_{1 \times 6} \right)^\top, & 6 \leq n \leq 10, k = n - 5 \\ \left(\mathbf{0}_{1 \times 5}, \mathbf{0}_{1 \times 5}, (\mathbf{R}_{m,k}^d)_{1 \times 6} \right)^\top, & 11 \leq n \leq 16, k = n - 10, \end{cases} \quad (44)$$

where $\mathbf{R}_{\alpha,k}^d$, $\alpha \in \{i, e\}$, is the k^{th} column vector of the 5×5 right eigenvector matrices \mathbf{R}_α^d of the flux jacobians $\frac{\partial \mathbf{f}_\alpha^d}{\partial \mathbf{U}_\alpha}$, and $\mathbf{R}_{m,k}^d$ is the k^{th} column vector of the right eigenvector matrix \mathbf{R}_m^d of the flux jacobian matrix $\frac{\partial \mathbf{f}_m^d}{\partial \mathbf{U}_m}$. The matrices \mathbf{R}_α^k and \mathbf{R}_m^k have the following expressions.

- For $d = x, y$, and $\alpha \in \{i, e\}$, the right eigenvector matrix \mathbf{R}_α^d is given by the relation,

$$\mathbf{R}_\alpha^d = \left(\frac{\partial \mathbf{U}_\alpha}{\partial \mathbf{W}_\alpha} \right) \mathbf{R}_{\alpha, \mathbf{W}}^d, \quad (45)$$

where the matrix $\mathbf{R}_{\alpha, \mathbf{W}}^d$ for $d = x$ is given by,

$$\mathbf{R}_{\alpha, \mathbf{W}}^x = \begin{pmatrix} \frac{1}{c_\alpha^2 h_\alpha} & 1 & 0 & 0 & \frac{1}{c_\alpha^2 h_\alpha} \\ \frac{-\sqrt{Q_\alpha^x}}{c_\alpha h_\alpha \Gamma_\alpha \rho_\alpha} & 0 & 0 & 0 & \frac{+\sqrt{Q_\alpha^x}}{c_\alpha h_\alpha \Gamma_\alpha \rho_\alpha} \\ \frac{(c_\alpha - \Gamma_\alpha \sqrt{Q_\alpha^x} u_{x\alpha}) u_{y\alpha}}{c_\alpha h_\alpha \Gamma_\alpha^2 \rho_\alpha (u_{x\alpha}^2 - 1)} & 0 & 1 & 0 & \frac{(c_\alpha + \Gamma_\alpha \sqrt{Q_\alpha^x} u_{x\alpha}) u_{y\alpha}}{c_\alpha h_\alpha \Gamma_\alpha^2 \rho_\alpha (u_{x\alpha}^2 - 1)} \\ \frac{(c_\alpha - \Gamma_\alpha \sqrt{Q_\alpha^x} u_{x\alpha}) u_{z\alpha}}{c_\alpha h_\alpha \Gamma_\alpha^2 \rho_\alpha (u_{x\alpha}^2 - 1)} & 0 & 1 & 0 & \frac{(c_\alpha + \Gamma_\alpha \sqrt{Q_\alpha^x} u_{x\alpha}) u_{z\alpha}}{c_\alpha h_\alpha \Gamma_\alpha^2 \rho_\alpha (u_{x\alpha}^2 - 1)} \\ 1 & 0 & 0 & 0 & 1 \end{pmatrix}. \quad (46)$$

- The eigenvector matrix \mathbf{R}_m^d for $d = x$ is given by,

$$\mathbf{R}_m^x = \begin{pmatrix} 0 & 0 & 1 & 0 & 0 & 0 \\ 0 & 1 & 0 & 0 & 0 & -1 \\ -1 & 0 & 0 & 0 & 1 & 0 \\ 0 & 0 & 0 & 1 & 0 & 0 \\ 1 & 0 & 0 & 0 & 1 & 0 \\ 0 & 1 & 0 & 0 & 0 & 1 \end{pmatrix}.$$

Remark A.1. For the y -directional flux, \mathbf{f}^y , we proceed similarly to get the set of eigenvalues Λ^y of the jacobian matrix $\frac{\partial \mathbf{f}^y}{\partial \mathbf{U}}$ as,

$$\Lambda^y = \left\{ \frac{(1 - c_i^2) u_{y_i} - (c_i / \Gamma_i) \sqrt{Q_i^y}}{1 - c_i^2 |\mathbf{u}_i|^2}, u_{y_i}, u_{y_i}, u_{y_i}, \frac{(1 - c_i^2) u_{y_i} + (c_i / \Gamma_i) \sqrt{Q_i^y}}{1 - c_i^2 |\mathbf{u}_i|^2}, \right. \\ \left. \frac{(1 - c_e^2) u_{y_e} - (c_e / \Gamma_e) \sqrt{Q_e^y}}{1 - c_e^2 |\mathbf{u}_e|^2}, u_{y_e}, u_{y_e}, u_{y_e}, \frac{(1 - c_e^2) u_{y_e} + (c_e / \Gamma_e) \sqrt{Q_e^y}}{1 - c_e^2 |\mathbf{u}_e|^2}, \right. \\ \left. -1, -1, 0, 0, 1, 1 \right\},$$

where, $Q_\alpha^y = 1 - u_{y_\alpha}^2 - c_\alpha^2 (u_{x_\alpha}^2 + u_{z_\alpha}^2)$, $\alpha \in \{i, e\}$. The corresponding right eigenvectors are given by fixing $d = y$ in the ordered set $\mathbf{R}_{\Lambda^d}^d = \{(\mathbf{R}_{\Lambda^d}^d)_n : n = 1, 2, 3, \dots, 16\}$ where $(\mathbf{R}_{\Lambda^d}^d)_n$ is defined by Eqn. (44) and the updated y -directional matrices $\mathbf{R}_{\alpha, \mathbf{W}}^y$ and \mathbf{R}_m^y are given by

$$\mathbf{R}_{\alpha, \mathbf{W}}^y = \begin{pmatrix} \frac{1}{c_\alpha^2 h_\alpha} & 1 & 0 & 0 & \frac{1}{c_\alpha^2 h_\alpha} \\ \frac{(c_\alpha - \Gamma_\alpha \sqrt{Q_\alpha^y} u_{y\alpha}) u_{x\alpha}}{c_\alpha h_\alpha \Gamma_\alpha^2 \rho_\alpha (u_{y\alpha}^2 - 1)} & 0 & 1 & 0 & \frac{(c_\alpha + \Gamma_\alpha \sqrt{Q_\alpha^y} u_{y\alpha}) u_{x\alpha}}{c_\alpha h_\alpha \Gamma_\alpha^2 \rho_\alpha (u_{y\alpha}^2 - 1)} \\ \frac{-\sqrt{Q_\alpha^y}}{c_\alpha h_\alpha \Gamma_\alpha \rho_\alpha} & 0 & 0 & 0 & \frac{+\sqrt{Q_\alpha^y}}{c_\alpha h_\alpha \Gamma_\alpha \rho_\alpha} \\ \frac{(c_\alpha - \Gamma_\alpha \sqrt{Q_\alpha^y} u_{y\alpha}) u_{z\alpha}}{c_\alpha h_\alpha \Gamma_\alpha^2 \rho_\alpha (u_{y\alpha}^2 - 1)} & 0 & 0 & 1 & \frac{(c_\alpha + \Gamma_\alpha \sqrt{Q_\alpha^y} u_{y\alpha}) u_{z\alpha}}{c_\alpha h_\alpha \Gamma_\alpha^2 \rho_\alpha (u_{y\alpha}^2 - 1)} \\ 1 & 0 & 0 & 0 & 1 \end{pmatrix}, \quad (47)$$

$$\mathbf{R}_m^y = \begin{pmatrix} 0 & -1 & 0 & 0 & 0 & 1 \\ 0 & 0 & 1 & 0 & 0 & 0 \\ 1 & 0 & 0 & 0 & -1 & 0 \\ 1 & 0 & 0 & 0 & 1 & 0 \\ 0 & 0 & 0 & 1 & 0 & 0 \\ 0 & 1 & 0 & 0 & 0 & 1 \end{pmatrix}. \quad (48)$$

511 A.2 Barth scaling and entropy scaled right eigenvectors

512 We ignore the superscript x to derive the entropy scaled right eigenvectors for the x -directional part; for
513 the y -directional flux, we proceed similarly. We have the entropy variable vector \mathbf{V}_α as

$$\mathbf{V}_\alpha = \begin{pmatrix} \frac{\gamma_\alpha - s_\alpha}{\gamma_\alpha - 1} + \beta_\alpha \\ u_{x_\alpha} \Gamma_\alpha \beta_\alpha \\ u_{y_\alpha} \Gamma_\alpha \beta_\alpha \\ u_{z_\alpha} \Gamma_\alpha \beta_\alpha \\ -\Gamma_\alpha \beta_\alpha \end{pmatrix}, \quad \text{where } \beta_\alpha = \frac{\rho_\alpha}{p_\alpha}.$$

We want to find scaling matrices \mathbf{T}_α^d ($d \in \{x, y\}$ and $\alpha \in \{i, e\}$) such that the scaled right eigenvector matrices $\tilde{\mathbf{R}}_\alpha^d = \mathbf{R}_\alpha^d \mathbf{T}_\alpha^d$, with \mathbf{R}_α^d as in Eqn. (45), satisfy

$$\frac{\partial \mathbf{U}_\alpha}{\partial \mathbf{V}_\alpha} = \tilde{\mathbf{R}}_\alpha^d (\tilde{\mathbf{R}}_\alpha^d)^\top.$$

The matrices \mathbf{T}_α^d are known as Barth scaling matrices. Following the procedure of [42], the scaling matrices \mathbf{T}_α^d are given by the square root of the matrices \mathbf{Y}_α^d where the expression for matrices \mathbf{Y}_α^d is given by the formulae

$$\mathbf{Y}_\alpha^d = (\mathbf{R}_{\alpha, \mathbf{w}}^d)^{-1} \frac{\partial \mathbf{W}_\alpha}{\partial \mathbf{V}_\alpha} \frac{\partial \mathbf{U}_\alpha}{\partial \mathbf{W}_\alpha}^{-\top} \mathbf{R}_{\alpha, \mathbf{w}}^d^{-\top},$$

where the matrices $\mathbf{R}_{\alpha, \mathbf{w}}^d$ are given by Eqn. (46) for $d = x$, and for the case $d = y$ the expressions for the matrices follows from Eqn. (47). Assuming $d = x$ for the clarity. A long simplification leads to the expressions

$$\mathbf{Y}_\alpha^x = \begin{pmatrix} \frac{c_\alpha^2 h_\alpha p_\alpha \left(1 + \frac{c_\alpha u_{x_\alpha}}{\Gamma_\alpha \sqrt{Q_\alpha^x}}\right)}{2\Gamma_\alpha (1 - c_\alpha^2 |\mathbf{u}|_\alpha^2)} & 0 & 0 & 0 & 0 \\ 0 & \frac{\rho_\alpha}{\Gamma_\alpha} \frac{\gamma_\alpha - 1}{\gamma_\alpha} & 0 & 0 & 0 \\ 0 & 0 & Y_{\alpha 33}^x & Y_{\alpha 34}^x & 0 \\ 0 & 0 & Y_{\alpha 43}^x & Y_{\alpha 44}^x & 0 \\ 0 & 0 & 0 & 0 & \frac{c_\alpha^2 h_\alpha p_\alpha \left(1 - \frac{c_\alpha u_{x_\alpha}}{\Gamma_\alpha \sqrt{Q_\alpha^x}}\right)}{2\Gamma_\alpha (1 - c_\alpha^2 |\mathbf{u}|_\alpha^2)} \end{pmatrix}$$

where, $Q_\alpha^x = 1 - u_{x_\alpha}^2 - c_\alpha^2(u_{y_\alpha}^2 + u_{z_\alpha}^2)$, $Y_{\alpha 33}^x = C_\alpha^x(1 - u_{x_\alpha}^2 - u_{y_\alpha}^2)$, $Y_{\alpha 44}^x = C_\alpha^x(1 - u_{x_\alpha}^2 - u_{z_\alpha}^2)$, $Y_{\alpha 34}^x = Y_{\alpha 43}^x = -C_\alpha^x u_{y_\alpha} u_{z_\alpha}$ and

$$C_\alpha^x = \frac{p_\alpha}{h_\alpha \Gamma_\alpha^3 \rho_\alpha^2 (1 - u_{x_\alpha}^2)}.$$

Consequently, the matrix $\mathbf{T}_\alpha^x = \sqrt{\mathbf{Y}_\alpha^x}$ is given by

$$\mathbf{T}_\alpha^x = \begin{pmatrix} \sqrt{\frac{c_\alpha^2 h_\alpha p_\alpha \left(1 + \frac{c_\alpha u_{x_\alpha}}{\Gamma_\alpha \sqrt{Q_\alpha^x}}\right)}{2\Gamma_\alpha (1 - c_\alpha^2 |\mathbf{u}|_\alpha^2)}} & 0 & 0 & 0 & 0 \\ 0 & \sqrt{\frac{\rho_\alpha}{\Gamma_\alpha} \frac{\gamma_\alpha - 1}{\gamma_\alpha}} & 0 & 0 & 0 \\ 0 & 0 & T_{\alpha 33}^x & T_{\alpha 34}^x & 0 \\ 0 & 0 & T_{\alpha 43}^x & T_{\alpha 44}^x & 0 \\ 0 & 0 & 0 & 0 & \sqrt{\frac{c_\alpha^2 h_\alpha p_\alpha \left(1 - \frac{c_\alpha u_{x_\alpha}}{\Gamma_\alpha \sqrt{Q_\alpha^x}}\right)}{2\Gamma_\alpha (1 - c_\alpha^2 |\mathbf{u}|_\alpha^2)}} \end{pmatrix}$$

where,

$$\begin{pmatrix} T_{\alpha 33}^x & T_{\alpha 34}^x \\ T_{\alpha 43}^x & T_{\alpha 44}^x \end{pmatrix} = \begin{cases} \begin{pmatrix} \sqrt{Y_{\alpha 33}^x} & 0 \\ 0 & \sqrt{Y_{\alpha 44}^x} \end{pmatrix} & \text{if } u_{y_\alpha} = u_{z_\alpha} = 0, \\ \sqrt{C_\alpha^x} \begin{pmatrix} \frac{u_{z_\alpha}^2 \sqrt{1 - u_{x_\alpha}^2} + \frac{u_{y_\alpha}^2}{\Gamma_\alpha}}{u_{y_\alpha}^2 + u_{z_\alpha}^2} & \frac{u_{y_\alpha} u_{z_\alpha}}{u_{y_\alpha}^2 + u_{z_\alpha}^2} \left(\frac{1}{\Gamma_\alpha} - \sqrt{1 - u_{x_\alpha}^2}\right) \\ \frac{u_{y_\alpha} u_{z_\alpha}}{u_{y_\alpha}^2 + u_{z_\alpha}^2} \left(\frac{1}{\Gamma_\alpha} - \sqrt{1 - u_{x_\alpha}^2}\right) & \frac{u_{y_\alpha}^2 \sqrt{1 - u_{x_\alpha}^2} + \frac{u_{z_\alpha}^2}{\Gamma_\alpha}}{u_{y_\alpha}^2 + u_{z_\alpha}^2} \end{pmatrix} & \text{otherwise.} \end{cases}$$

Remark A.2. Proceeding similarly in the y -direction with the matrix $\mathbf{R}_{\alpha, \mathbf{W}}^y$ as in Eqn. (47), the scaling matrix is given by

$$\mathbf{T}_{\alpha}^y = \begin{pmatrix} \sqrt{\frac{c_{\alpha}^2 h_{\alpha} p_{\alpha} \left(1 + \frac{c_{\alpha} u_{y_{\alpha}}}{\Gamma_{\alpha} \sqrt{Q_{\alpha}^y}}\right)}{2\Gamma_{\alpha}(1-c_{\alpha}^2 |\mathbf{u}_{\alpha}^2|)}} & 0 & 0 & 0 & 0 \\ 0 & \sqrt{\frac{\rho_{\alpha}}{\Gamma_{\alpha}}} \frac{\gamma_{\alpha}-1}{\gamma_{\alpha}} & 0 & 0 & 0 \\ 0 & 0 & T_{\alpha 33}^y & T_{\alpha 34}^y & 0 \\ 0 & 0 & T_{\alpha 43}^y & T_{\alpha 44}^y & 0 \\ 0 & 0 & 0 & 0 & \sqrt{\frac{c_{\alpha}^2 h_{\alpha} p_{\alpha} \left(1 - \frac{c_{\alpha} u_{y_{\alpha}}}{\Gamma_{\alpha} \sqrt{Q_{\alpha}^y}}\right)}{2\Gamma_{\alpha}(1-c_{\alpha}^2 |\mathbf{u}_{\alpha}^2|)}} \end{pmatrix}$$

where, $Q_{\alpha}^y = 1 - u_{y_{\alpha}}^2 - c_{\alpha}^2(u_{x_{\alpha}}^2 + u_{z_{\alpha}}^2)$, and the block entries are given by the matrices

$$\begin{pmatrix} T_{\alpha 33}^y & T_{\alpha 34}^y \\ T_{\alpha 43}^y & T_{\alpha 44}^y \end{pmatrix} = \begin{cases} \begin{pmatrix} \sqrt{Y_{\alpha 33}^y} & 0 \\ 0 & \sqrt{Y_{\alpha 44}^y} \end{pmatrix} & \text{if } u_{x_{\alpha}} = u_{z_{\alpha}} = 0, \\ \sqrt{C_{\alpha}^y} \begin{pmatrix} \frac{u_{z_{\alpha}}^2 \sqrt{1-u_{y_{\alpha}}^2} + \frac{u_{x_{\alpha}}^2}{\Gamma_{\alpha}}}{u_{x_{\alpha}}^2 + u_{z_{\alpha}}^2} & \frac{u_{x_{\alpha}} u_{z_{\alpha}}}{u_{x_{\alpha}}^2 + u_{z_{\alpha}}^2} \left(\frac{1}{\Gamma_{\alpha}} - \sqrt{1-u_{y_{\alpha}}^2} \right) \\ \frac{u_{x_{\alpha}} u_{z_{\alpha}}}{u_{x_{\alpha}}^2 + u_{z_{\alpha}}^2} \left(\frac{1}{\Gamma_{\alpha}} - \sqrt{1-u_{y_{\alpha}}^2} \right) & \frac{u_{x_{\alpha}}^2 \sqrt{1-u_{y_{\alpha}}^2} + \frac{u_{z_{\alpha}}^2}{\Gamma_{\alpha}}}{u_{x_{\alpha}}^2 + u_{z_{\alpha}}^2} \end{pmatrix} & \text{otherwise,} \end{cases}$$

with $Y_{\alpha 33}^y = C_{\alpha}^y(1 - u_{y_{\alpha}}^2 - u_{x_{\alpha}}^2)$, $Y_{\alpha 44}^y = C_{\alpha}^y(1 - u_{y_{\alpha}}^2 - u_{z_{\alpha}}^2)$ and

$$C_{\alpha}^y = \frac{p_{\alpha}}{h_{\alpha} \Gamma_{\alpha}^3 \rho_{\alpha}^2 (1 - u_{y_{\alpha}}^2)}.$$

B ARK3-IMEX coefficients table

The coefficients for the third order ARK-IMEX time update are given as follows,

		$l = 0$	$l = 1$	$l = 2$	$l = 3$
$a_{ml}^{[NS]}$	$m = 1$	$\frac{1767732205903}{2027836641118}$	0	0	0
	$m = 2$	$\frac{5535828885825}{10492691773637}$	$\frac{788022342437}{10882634858940}$	0	0
	$m = 3$	$\frac{6485989280629}{16251701735622}$	$-\frac{4246266847089}{9704473918619}$	$\frac{10755448449292}{10357097424841}$	0
$a_{ml}^{[S]}$	$m = 1$	$\frac{1767732205903}{4055673282236}$	$\frac{1767732205903}{4055673282236}$	0	0
	$m = 2$	$\frac{2746238789719}{10658868560708}$	$-\frac{640167445237}{6845629431997}$	$\frac{1767732205903}{4055673282236}$	0
	$m = 3$	$\frac{1471266399579}{7840856788654}$	$-\frac{4482444167858}{7529755066697}$	$\frac{11266239266428}{11593286722821}$	$\frac{1767732205903}{4055673282236}$
$b_l^{[NS]}$		$\frac{1471266399579}{7840856788654}$	$-\frac{4482444167858}{7529755066697}$	$\frac{11266239266428}{11593286722821}$	$\frac{1767732205903}{4055673282236}$
$b_l^{[S]}$		$\frac{2756255671327}{12835298489170}$	$-\frac{10771552573575}{22201958757719}$	$\frac{9247589265047}{10645013368117}$	$\frac{2193209047091}{5459859503100}$
c_l		0	$\frac{1767732205903}{2027836641118}$	$\frac{3}{5}$	1

Table 5: The coefficients for ARK3-IMEX time update scheme.